

# Optical and electrical properties of thermochromic VO<sub>2</sub> thin film combined with Au or Zr-containing compounds nanoparticles

G. Savorianakis<sup>a,b</sup>, N. Martin<sup>c</sup>, A.J. Santos<sup>d,e,\*</sup>, J. J. Jiménez<sup>d,e</sup>, M. Dominguez<sup>e,f</sup>, F.M. Morales<sup>d,e</sup>, M. Protsak<sup>g</sup>, A. Choukourov<sup>g</sup>, M. Voué<sup>b</sup> and S. Konstantinidis<sup>a,\*</sup>

<sup>a</sup> *Plasma-Surface Interaction Chemistry (ChIPS), Research Institute for Materials Science and Engineering, University of Mons, 20 Place du Parc, Mons B-7000, Belgium.*

<sup>b</sup> *Physics of Materials and Optics Group (LPMO), Research Institute for Materials Science and Engineering, University of Mons, 20 Place du Parc, Mons B-7000, Belgium.*

<sup>c</sup> *SUPMICROTECH, CNRS, Institut FEMTO-ST, 25000 Besançon Cedex, France.*

<sup>d</sup> *Department of Materials Science and Metallurgic Engineering, and Inorganic Chemistry, Faculty of Sciences, University of Cádiz, 11510 Puerto Real, Cádiz, Spain.*

<sup>e</sup> *IMEYMAT: Institute of Research on Electron Microscopy and Materials, University of Cádiz, 11510 Puerto Real, Spain.*

<sup>f</sup> *Department of Condensed Matter Physics, Faculty of Sciences, University of Cádiz, 11510 Puerto Real, Cádiz, Spain.*

<sup>g</sup> *Department of Macromolecular Physics, Faculty of Mathematics and Physics, Charles University, V Holešovičkách 2, Prague, Czech Republic.*

\* Corresponding author: [antonio.santos@uca.es](mailto:antonio.santos@uca.es); [stephanos.konstantinidis@umons.ac.be](mailto:stephanos.konstantinidis@umons.ac.be)

**Abstract:** In this study, we investigate the influence of metal-based nanoparticles (NPs), namely Au and ZrN, on the optical and electrical characteristics of thermochromic vanadium dioxide (VO<sub>2</sub>) thin films. Au NPs are prepared by wet

chemistry-based methods and are chemically bonded to the VO<sub>2</sub> surface via organic linkers, while ZrN NPs are synthesized by gas aggregation technique and deposited on the VO<sub>2</sub> layer, eventually leading to the formation of additional Zr-containing compounds (e.g., nitrides, oxides and/or oxynitrides). Two configurations were then investigated: i) NPs deposited on the VO<sub>2</sub> surface and ii) NPs embedded inside the VO<sub>2</sub> layer. The combination of Au or ZrN NPs with the VO<sub>2</sub> surface results in enhanced infrared light modulation, attributed to anti-reflection effects induced by the presence of the NPs layer on the VO<sub>2</sub> surface. On the other hand, the average metal-to-insulator transition temperature is significantly reduced down to 35.5°C when Au NPs are embedded in the VO<sub>2</sub> layer. This is attributed to electron-doping effects and confirmed by the resistivity and optical measurements. Finally, analysis of optical performance parameters such as solar energy modulation, infrared transmittance and luminous transmittance in the visible range provides insights into the overall capabilities of these materials for smart window applications. Furthermore, stability assessments show consistent results over temperature cycles, highlighting the reliability of these nanocomposite platforms. This study introduces a dual-configuration approach to modulate the thermochromic response of VO<sub>2</sub> using metal-based nanoparticles, revealing a clear structure–property relationship depending on NP placement and composition.

**Keywords:** Vanadium dioxide; thin films; thermochromism; metal nanoparticles; smart windows; metal-to-insulator transition; optical properties; energy efficiency.

## 1. Introduction

Thermochromic materials are characterized by a distinctive metal-to-insulator transition (MIT), driven by reversible changes in their crystalline structure in response to temperature variations[1–3]. Among these, (monoclinic) vanadium dioxide ( $\text{VO}_2$ ) has garnered significant attention due to its pronounced and reversible changes in electrical, magnetic, and optical properties, which occur at a relatively moderate temperature of  $T_{MIT} = 68^\circ\text{C}$ . Thin films of  $\text{VO}_2$  have thus emerged as exceptional candidates for a wide array of technological applications, including smart windows[4–7], fiber optic switches[8–11], and sensors[12–14]. The observed transition properties of  $\text{VO}_2$  are notably sensitive to a variety of factors, including the growth technique[15], crystal size[16], annealing conditions[17], doping[18], and induced strain[19,20].

In recent years, research has increasingly focused on the modulation of the switching characteristics of thermochromic  $\text{VO}_2$  through others pathways. In this respect, the incorporation of plasmonic metal nanoparticles (NPs) such as silver (Ag)[21], gold (Au)[22,23], and platinum (Pt)[24] have demonstrated distinct effects on optical hysteresis and variations in  $T_{MIT}$ , avoiding doping as a necessary modulation element and highlighting the potential of plasmonic effects in fine-tuning the functional properties of  $\text{VO}_2$ . Interestingly, plasmon resonance modulation by the  $\text{VO}_2$  phase transition has also been reported for Au– $\text{VO}_2$  systems[23], emphasizing the multifaceted interactions between metal NPs and the thermochromic matrix. Going beyond the state-of-the-art, the use of transition metal nitride NPs such as zirconium nitride (ZrN), alongside with Au NPs, is justified for various reasons related to their unique properties. Indeed, recent advances in nanoplasmonics, including high-temperature[25,26], light-harvesting[27], and thermoplasmonic[28,29] applications, led to significant interest in these transition metal nitride nanoparticles (e.g., TiN, ZrN, and

HfN). They offer the following three main advantages: (i) plasmonic properties comparable to those of gold[6,30], (ii) tunability via the metal/nitrogen stoichiometry during the synthesis[26], and (iii) refractory character[31,32], enabling high-temperature operation (melting points of TiN and ZrN are 2930 °C and 2952 °C, respectively, versus 1064 °C for Au [33]) and cost-effectiveness. This crucial feature makes it possible to use the NPs where the operating temperature of the plasmonic device is high. Economically speaking, ZrN NPs are the least expensive, especially compared to gold, and therefore, they were chosen for the purpose of this research.

In the present study, we integrate plasmonic Au or ZrN nanoparticles (NPs) either into or onto a VO<sub>2</sub> thin film (Fig. 1) to tailor the nanocomposite's optoelectronic properties by taking advantage of the plasmonic resonances of Au and ZrN in the visible and near-IR range. We anticipate a distinct behavior when the plasmonic NPs are fully embedded within the VO<sub>2</sub> film compared to being deposited on its surface. In a previous work[34], we highlighted the importance of NP positioning and the effective contact area between plasmonic NPs and the VO<sub>2</sub> matrix in determining the plasmon resonance peak wavelength.

Unlike previous studies that explored doping the VO<sub>2</sub> lattice, our work compares these two configurations, allowing systematic assessment of the effects of NP position, density, and chemical nature. This approach provides deeper insight into the physical mechanisms at the VO<sub>2</sub>/NP interface and offers new strategies for optimizing VO<sub>2</sub>-based materials in advanced applications. To the best of our knowledge, this is the first systematic comparison of VO<sub>2</sub> thin films hybridized with plasmonic Au and ZrN nanoparticles, both on the surface and embedded within the layer, to assess their impact on optical modulation and transition temperature.

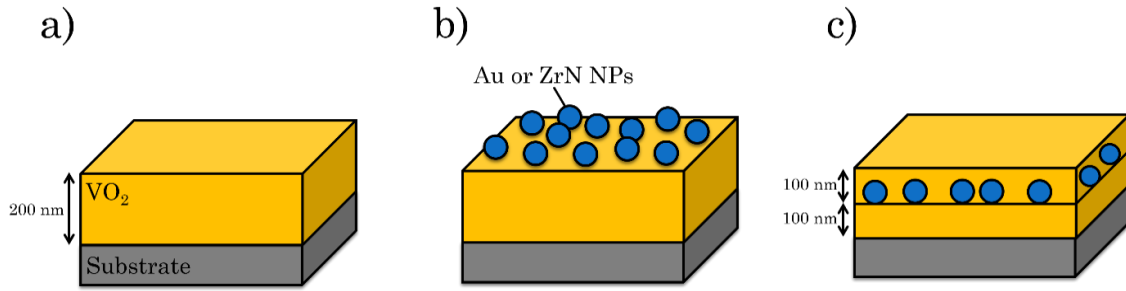


**Fig. 1.** Schematic view of platforms studied: (a) 200 nm thick VO<sub>2</sub>, (b) 200 nm thick NPs/VO<sub>2</sub> and (c) VO<sub>2</sub>/NPs/VO<sub>2</sub>.

## 2. Materials and Methods

### 2.1. Thermochromic VO<sub>2</sub> Film Deposition

Deposition was carried out using a low-pressure plasma-based reactive direct current (DC) magnetron sputtering process. A vanadium target 2 inches in diameter and 0.25 inches thick (99.99% purity) was used. Prior to deposition, a turbomolecular pump supported by a dry pump achieved a residual pressure of  $\sim 1 \times 10^{-6}$  Pa. For the synthesis of the vanadium oxide thin films, a mixture of argon and oxygen was introduced into the chamber at a constant working pressure of 1 mTorr (0.13 Pa) and a constant discharge current of 0.3 A. Throughout the deposition, the flux of argon and oxygen remained fixed at 8 and 1.2 sccm (standard cubic centimeter per minute), respectively. The sample was subsequently annealed for 45 minutes at 500°C in a pure oxygen atmosphere (at a pressure of around 400 Pa) in the same chamber to induce film crystallization and oxidation in order to produce the VO<sub>2</sub> monoclinic phase, which is thermochromic. The substrate consisted of (100) single crystal silicon wafers or BK7 glass cleaned with a detergent solution (3% v/v RBS in water, Chemical Products R. Borghgraef S.A.).

## 2.2. Synthesis and grafting of Au NPs

To produce gold nanoparticles (Au NPs), we used a Turkevich approach with slight modifications. Specifically, we heated 99 mL of a 0.0025 M  $\text{HAuCl}_4$  aqueous solution to its boiling point ( $100^\circ\text{C}$ ) and then added 1 mL of a 0.0388 M sodium citrate ( $\text{Na}_3\text{Cit}$ ) solution to induce the chemical reduction of gold(III) chloride trihydrate[35]. The resulting reddish solution containing Au NPs was cooled to room temperature over a period of 15 minutes, and  $25\pm 5$  nm NPs were synthesized.

In order to functionalize the 200 nm-thick  $\text{VO}_2$  thin films and create a hybrid platform based on NPs onto the  $\text{VO}_2$  surface, labeled as "NPs/ $\text{VO}_2$ ," a protocol inspired by different studies was set up[36–38]. Our goal is to promote the formation of a monolayer of well-dispersed Au NPs on the surface of  $\text{VO}_2$  film. Firstly, the thermochromic  $\text{VO}_2$  films were immersed in acetone and methanol in an ultrasonic bath for 10 minutes to generate additional reactive hydroxyl groups on the surface. Activated  $\text{VO}_2$  thin films were then immersed in the linker solution for the required duration. The linker was prepared with an APTMS (3-Aminopropyl)trimethoxysilane) solution in methanol at a concentration of 5 % (v/v). To finish, samples were dipped in an NPs solution to promote the reaction of gold with the amine group of APTMS. The functionalized  $\text{VO}_2$  was rinsed with water to eliminate any remaining unattached NPs. For the production of the platform with NPs embedded inside a  $\text{VO}_2$  matrix, " $\text{VO}_2/\text{NPs}/\text{VO}_2$ ," another process was adopted. Initially, a layer of  $\text{VO}_x$  100 nm thick, that is to say, an as-deposited film, was synthesized using the exact same deposition parameters as the previous platform. At that time, the annealing had not yet been carried out, which was the only distinction. Next, the Au NPs were grafted using the same APTMS methodology. Lastly, Au NPs were covered with a second layer of 100 nm

VO<sub>x</sub>. The sample was then annealed under the same parameters as NPs/VO<sub>2</sub>, and the VO<sub>2</sub>/NPs/VO<sub>2</sub> platform was created. This procedure was executed in order to prevent annealing the sample twice: Once for the first 100 nm layer and a second time for the layer on top. This would have promoted the formation of V<sub>2</sub>O<sub>5</sub> rather than VO<sub>2</sub> in the first layer due to sequential heat treatments[39].

Au NPs can also be deposited via magnetron sputtering with an Au target, stopping the film growth before the coalescence step. Au atoms condense on the substrate surface, forming clusters that grow into NPs. The size and spatial distribution of these NPs depend on factors like gas pressure, substrate temperature, deposition rate, and substrate-target distance. The APTMS method offers advantages over magnetron sputtering, such as precise and uniform control of NP distribution on VO<sub>2</sub>, tunable by dipping time. It also improves NP adhesion and stability due to covalent bonds, making the NPs more durable and resistant to annealing compared to the physical adhesion in sputtering.

### **2.3. ZrN NPs synthesised by GAS**

The generation of ZrN nanoparticles was performed using a gas aggregation cluster source integrated into the primary vacuum chamber. Rotary and diffusion pumps were used to evacuate the deposition system to a pressure of 10<sup>-6</sup> Torr. The GAS system consists of a cylindrical, water-cooled chamber with a conical nozzle and a focalizing orifice (4 mm diameter, 2 cm length) at the end. It is also equipped with a 3-inch DC magnetron Zr target. The ZrN NPs were obtained by sputtering in an Ar/N<sub>2</sub> gas mixture. Sputtering process was carried out in Ar set at 6.00 sccm with 0.26 sccm of N<sub>2</sub> reaching a total pressure of 38 Pa with a magnetron current fixed at 500 mA. The N<sub>2</sub> concentration just before the poisoning was chosen as the target regime. Although an Ar/N<sub>2</sub> mixture is employed during the deposit, elemental mapping by Scanning

transmission electron microscopy - Energy-dispersive X-ray (STEM-EDX) measurement in previous studies exhibits a core-shell structure composition with ZrN core enveloped by an oxynitride shell of approximately 2 nm[40]. However, it was discovered that Zr and N have equal distributions across the whole NP volume, except for the oxidized outermost layer. The EDX and XPS results demonstrate that when ZrN NPs are exposed for one day to air, they are susceptible to a partial oxidation process inducing the production of ZrO<sub>2</sub> and ZrON. In addition, Density functional theory (DFT) calculations of ZrN density of states with different amounts of oxygen substitutions show that ZrN with a slight oxidation remains metallic, but for ZrN<sub>0.7</sub>O<sub>1.3</sub>, a band gap of 2.2 eV and a semiconductor state appear.

#### **2.4. Film Characterization**

The crystalline structure was determined by grazing incidence X-ray diffraction (GIXRD) analysis using a Panalytical Empyrean system with a Cu K $\alpha$  source at 1.5406 Å. The X-ray source voltage was set at 45 kV and the angle of incidence of the X-ray beam was maintained at 1° relative to the sample holder surface. The Scherrer equation was used to evaluate the grain size with  $D = \frac{0.9\lambda}{\alpha \cos \theta}$ , where D is the mean size of the crystalline domains (Å),  $\lambda$  is the X-ray wavelength (Å),  $\alpha$  is the line broadening at half the maximum intensity (rad), and  $\theta$  is the Bragg diffraction angle (°). Raman spectroscopy was performed using a Bruker Senterra spectrometer equipped with a CCD detector and a HeNe laser (532 nm) emitting at 20 mW. Transmittance spectra were obtained using a PerkinElmer Lambda 900 UV/VIS/NIR Spectrometer equipped with a THMS600 Linkam stage for temperature control. Vis-NIR transmittance spectra were recorded in the wavelength range of 350–2500 nm at selected temperatures in the range of 25–100°C. For the dynamic monitoring of the thermally induced phase transition, the thermal evolution of the optical transmittance at a selected NIR



wavelength (2500 nm) was observed in both heating and cooling cycles at a controlled rate of  $5^{\circ}\text{C min}^{-1}$ . Measurements of  $\text{VO}_2$  films DC electrical resistivity according to temperature were carried out in a customized chamber utilizing the four-probe gold-coated tips in a van der Pauw geometry. For all cycles in temperature, the THMS600 Linkam platform was used with a  $1^{\circ}\text{C min}^{-1}$  ramp from  $25^{\circ}\text{C}$  to  $100^{\circ}\text{C}$  and then back to  $25^{\circ}\text{C}$  using the same negative ramp. Carrier mobility and carrier concentration were obtained by Hall effect using the van der Pauw geometry. A magnetic field of 0.8 T was applied perpendicular to the sample surface. The same heating-cooling rate was used as before, i.e.,  $1^{\circ}\text{C min}^{-1}$ . A field emission gun scanning electron microscope (FEG-SEM Hitachi SU8020) with a 5 kV acceleration voltage was used to obtain high-magnification SEM images of the samples.

In order to carry out further characterizations of the samples by scanning and scanning-transmission electron microscopy techniques, samples were processed to obtain suitable electron-transparent preparations using either focused-ion beam (FIB) in a Thermo Scientific Scios 2 DualBeam system, or tripod polishing[41–43] plus uncooled, soft  $\text{Ar}^+$  ion-milling (i.e. 3-3.5 keV) in a Gatan model 691 precision ion polishing system (PIPS). The latter was selected for the sample with Au NPs inside the  $\text{VO}_2$  layer since after one attempt using FIB, the resulting lamella seemed to come from an empty area with no visible NPs, so this technique was applied subsequently as an alternative to have a larger amount of observable, electron-transparent material[44] and thus a higher chance to find these nanostructures. Regarding the studies of these samples by (S)TEM, they were carried out using either a Thermo Scientific Talos F200X or a Talos X200 microscope, both operated at an acceleration voltage of 200 kV. Atomic Force Microscopy (AFM) images were obtained using a Bruker MultiMode 8-HR AFM

system. A SiN probe (PFQNE-AL, 5 nm tip radius) was used for all imaging. Images were processed with Gwyddion software.

### 3. Results and discussion

#### 3.1. Characterization of bare VO<sub>2</sub> thin films

**Fig. 2** shows the Raman spectrum (a) and GIXRD diffractogram (b) for a 200 nm thin film deposited with optimized conditions. Concerning the Raman spectra, the film exhibits monoclinic VO<sub>2</sub> vibration modes at 139, 193, 224, 264, 307, 389, 389, 499, 613 and 825 cm<sup>-1</sup>. A single peak corresponding to V<sub>3</sub>O<sub>7</sub> at 883 cm<sup>-1</sup> also appears. Following that, GIXRD measurement is also performed to evaluate the crystalline constitution of our sample grown with optimized conditions. Except for diffraction peaks characteristic of the monoclinic VO<sub>2</sub> phase, there are no diffraction lines related to other oxidation states. The diffractogram shows highly oriented films and different crystalline phase orientations. The weak V<sub>3</sub>O<sub>7</sub> Raman mode likely arises from trace, poorly crystalline oxide at the film surface or grain boundaries, which falls below the GIXRD detection limit and may overlap with VO<sub>2</sub> diffraction peaks. Using the Scherrer equation on three peaks, the crystallite size is 20.1 ± 1.7 nm.

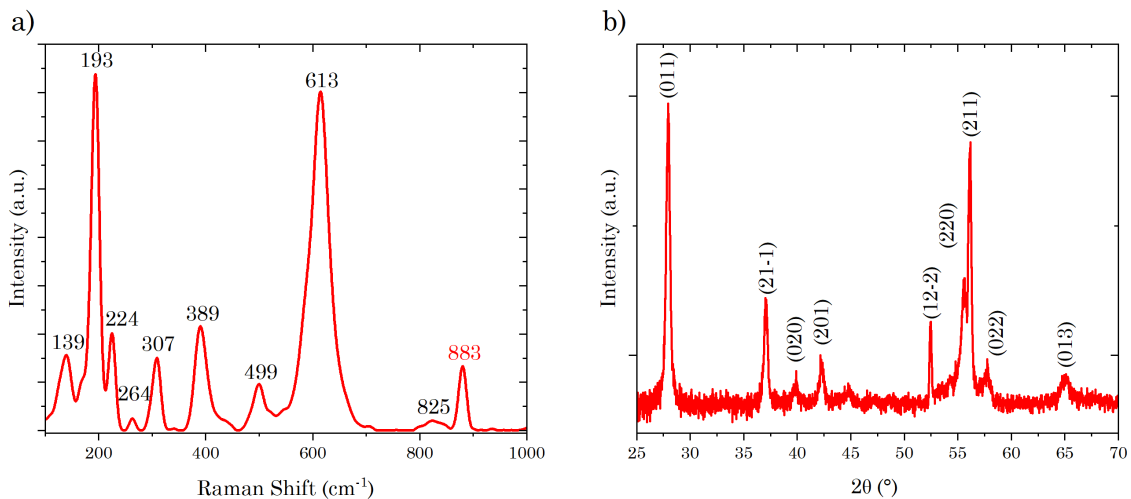


**Figure 2.** Raman spectra (a) and GIXRD diffractogram (b) of the 200 nm thick vanadium oxide thin films at room temperature. Black and red labels on Raman spectrum refer to monoclinic VO<sub>2</sub>[45] and V<sub>3</sub>O<sub>7</sub>[46], respectively. GIXRD data correspond to the monoclinic VO<sub>2</sub> phase, coming from JCPD 00-009-0142 card and[47].

Now that the elaboration of monoclinic VO<sub>2</sub> film has been confirmed, the thermochromic behavior can be investigated. For this purpose, the optical characterization of the coating was carried out between 25°C (in the so-called "cold" state) and 100°C (in the "hot" state), which is illustrated in **Fig. 3**. Transmittance spectra (**Fig. 3(a)**) show optical modulations of about 18% in the infrared range once the material is in the hot state. The latter being characteristic of the MIT of monoclinic VO<sub>2</sub>. In the visible range only, slight variation is observed. However, the low-temperature spectrum describes an unusual trend compared to that of pure VO<sub>2</sub>, with higher transmittance values in the visible range than in the near-infrared, and a maximum transmittance peak near 600–700 nm. According to previous studies[48], this is indicative of the coexistence of VO<sub>2</sub> with other VO<sub>2+x</sub> compounds, which is consistent with what was previously evidenced by Raman spectroscopy (VO<sub>2</sub> + V<sub>3</sub>O<sub>7</sub>). For the same sample, the optical transmittance is measured as a function of temperature while keeping the wavelength fixed at 2500 nm, to characterize the hysteresis behavior (**Fig. 3(b)**). To study the hysteresis in detail, the first-order derivative was calculated to determine accurately the transition temperature  $T_{MIT}$  (see **Figure S1** in Supplementary Material Section I). The heating ( $T_{heat}$ ) and cooling ( $T_{cool}$ ) transition temperatures are 70.0 °C and 57.4 °C, respectively. Calculating the difference between these two values allows determining the width of the hysteresis, which equals

22.6°C. Furthermore, the temperature  $T_{MIT}$ , calculated by averaging  $T_{heat}$  and  $T_{cool}$ , is 63.7°C. The observed transition characteristics of VO<sub>2</sub> show significant variability and are influenced by factors such as growth technique, annealing, doping, crystal size, strain and vacancies. The literature shows that larger grain size and fewer structural defects (improving crystal quality) result in a smaller hysteresis width accompanied by an enlarged variation of the optical properties of the material as it switches from the cold to the hot state, and viceversa[3]. Hysteresis widths equal to 3[49], 12[50] and 18°C[51] can be measured for VO<sub>2</sub> thin films synthesized by reactive magnetron sputtering with other deposition parameters.

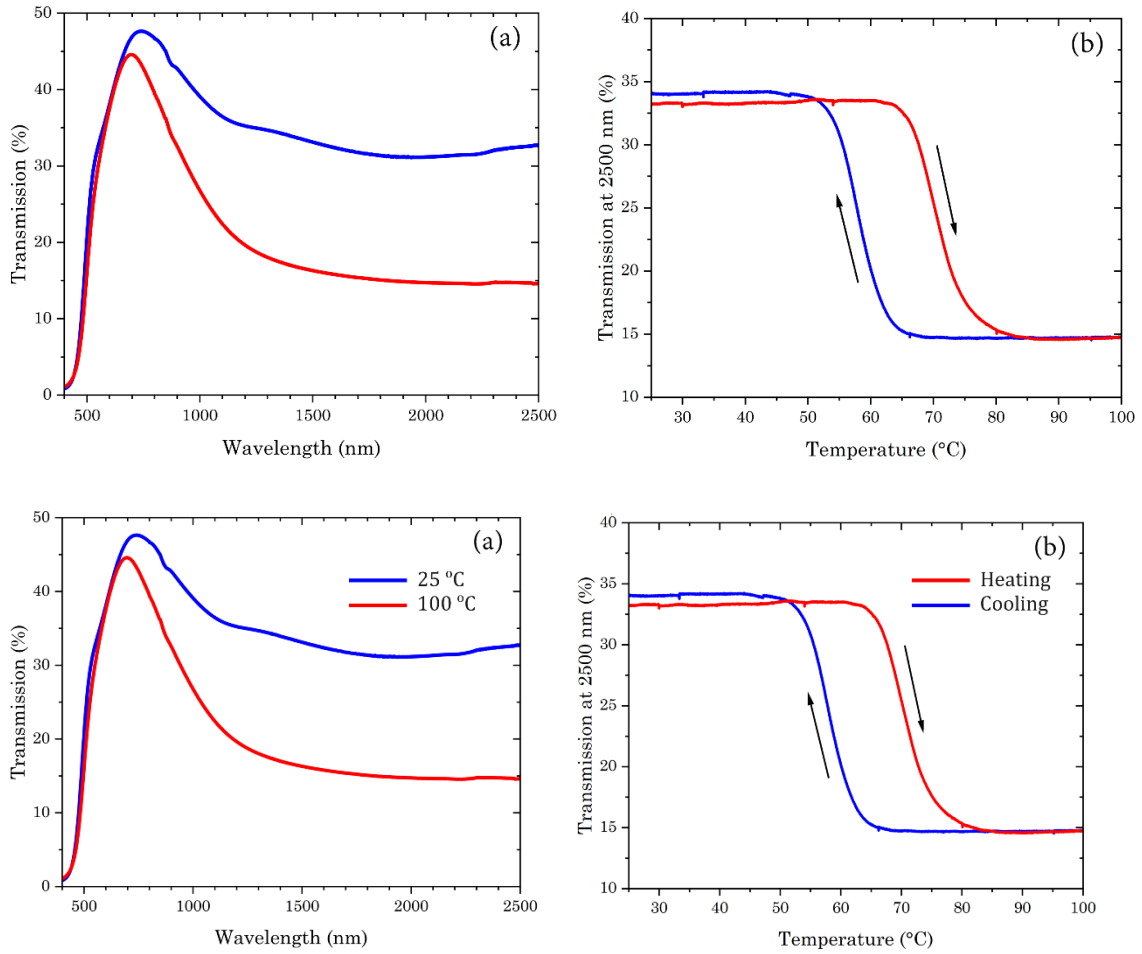


**Fig. 3.** (a) Transmittance spectra of a 200 nm-thick VO<sub>2</sub> film on glass at 25°C (blue) and 100°C (red). (b) Thermal hysteresis loop for a monoclinic 200 nm-thick VO<sub>2</sub> film deposited on glass and obtained thanks to a transmittance measurement while keeping the wavelength at 2500 nm.

Another type of thin film analysis can be carried out to characterize sample's electronic transport properties, namely carrier mobility and concentration (**Fig. 4**). In the case of thermochromic VO<sub>2</sub> films, resistivity measurements as a function of temperature have been widely studied in the literature, demonstrating the switching between insulator and metallic behavior straightforwardly[52,53]. As shown in **Fig. 4(a)**, the thermal loop on the sheet resistivity exhibits a jump of about 1 order of magnitude, driven by the switching between the two distinct VO<sub>2</sub> crystalline phases (monoclinic to tetragonal structure). By calculating the first-order derivative (refer to Fig. S2 in Supplementary Material Section I), the hysteresis characteristics calculated as the width or cooling and heating transition temperature are similar to those obtained from the optical transmittance measurement.

In addition to the sheet resistivity measurement, Hall analysis was carried out to study the temperature variations of the free carrier density and electron mobility (**Fig. 4(b–c)**). As the temperature increases, the mobility of the carriers is equivalent to  $8 \times 10^{-5} \text{ m}^2 \text{V}^{-1} \text{s}^{-1}$  when the concentration remains around  $1 \times 10^{25} \text{ m}^{-3}$ . Before the transition temperature, a peak ( $2 \times 10^{-3} \text{ m}^2 \text{V}^{-1} \text{s}^{-1}$ ) appears for the charge carrier concentration, while a dip ( $1 \times 10^{24} \text{ m}^{-3}$ ) appears for the concentration. These sharp and noisy transitions of carrier concentration and mobility vs. temperature correlate with resistivity and optical transmission variations. They have ever been reported by others[54,55]. In addition,

Yang *et al.*[56] similarly pointed out beating phenomena of electronic transport properties during MIT of VO<sub>2</sub> epitaxial thin films. They mainly assigned it to displacement of the four probes during measurements. Although these technical drawbacks cannot be completely rules out for our data, abrupt changes of  $\mu$  and  $n$  are also related to unstable scattering of carriers by the metallic phase and insulating boundaries [57]. Reaching the heating transition temperature, the mobility stabilizes at the same value as before the transition. In contrast, the final value of the carrier concentration after the transition is higher by one order of magnitude. This result indicates that carrier concentration is the main parameter governing the resistivity jump between the cold and hot states of thermochromic VO<sub>2</sub>. The mobility peak around  $T_{MIT}$  is mainly due to electron diffusion from the high temperature zone (metallic) to the low temperature zone (insulator) when the MIT transition occurs[57]. In fact, Qazilbash et al. have shown by scanning near-field infrared microscopy that throughout the VO<sub>2</sub> phase change, metallic isolated puddles first appear and eventually merge to form a fully metallic film[58]. During this coexistence regime, carrier trapping at insulator–metal interfaces and preferential conduction through nascent metallic pathways yield a transient dip in the net free-carrier concentration alongside a mobility peak

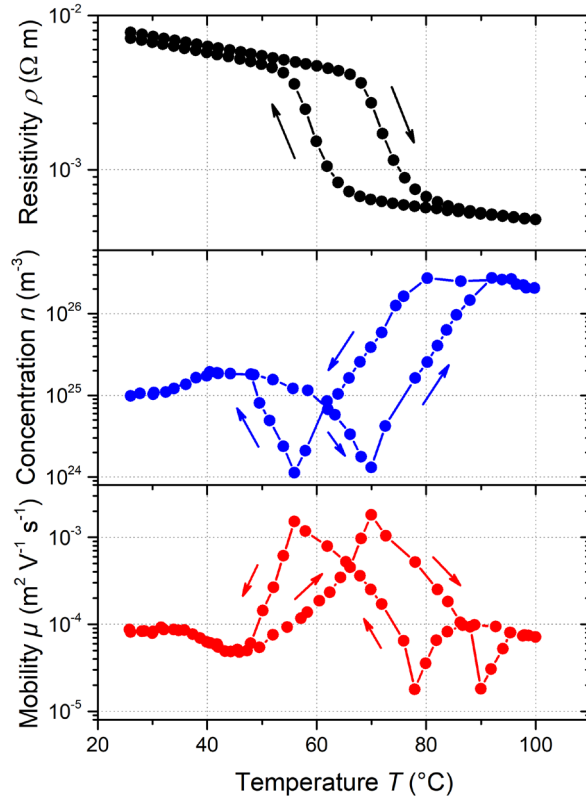


**Figure 4.** (a) Thermal hysteresis loop of sheet resistivity hysteresis and Hall Effect measurement, giving (b) carrier mobility and (c) carrier concentration, as a function of temperature for a monoclinic 200 nm thick VO<sub>2</sub> film deposited on glass.

### 3.2. Study of NPs/VO<sub>2</sub> hybrid thin films

A 200 nm-thick VO<sub>2</sub> layer is first deposited on glass according to the protocol described in section 2.2. The resulting surface of sample VO<sub>2</sub>/Au can be observed in **Fig. 5(a)**, which shows a plain-view SEM image. This figure evidences a reasonably homogeneous coverage of the VO<sub>2</sub> surface with Au NPs, which are easily identified as tiny and seemingly sphere-shaped bright features. Further analysis indicates that this layer is present everywhere on the VO<sub>2</sub> films. This result demonstrates the efficiency of the APTMS protocol to graft a monolayer of NPs on a VO<sub>2</sub> surface.

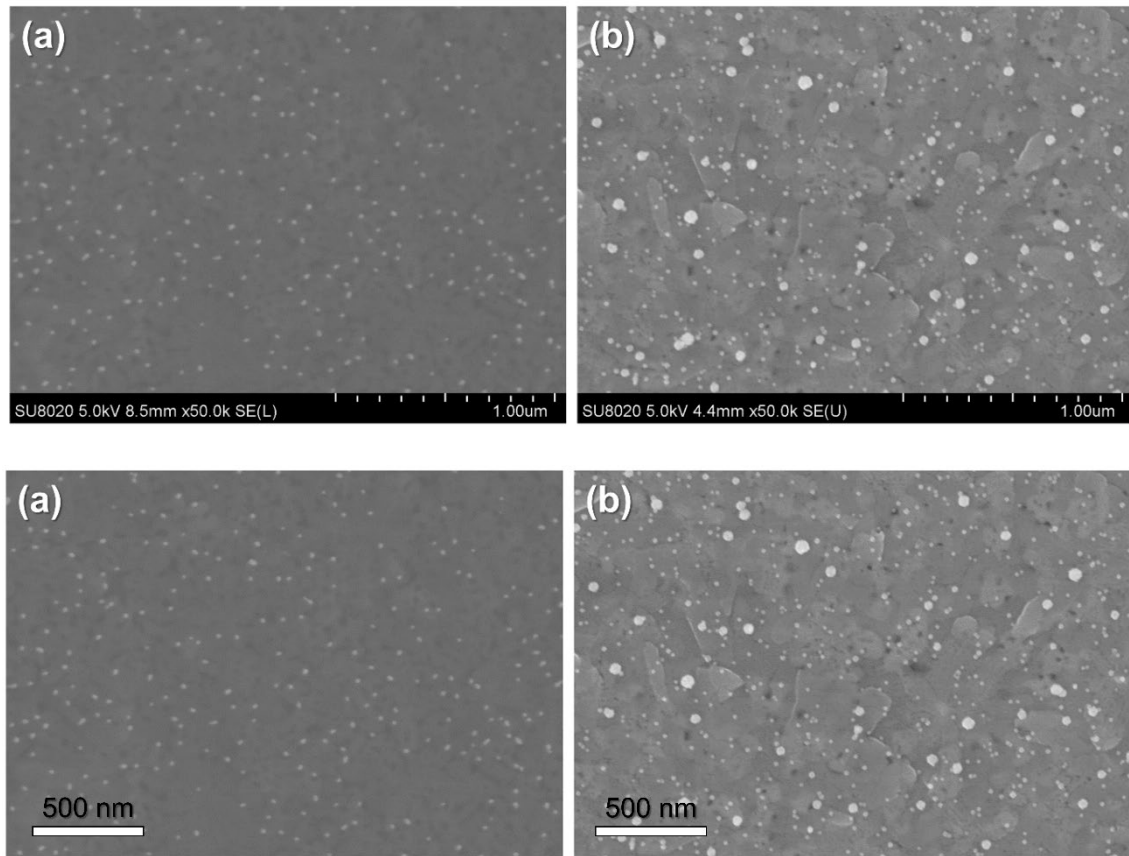


**Fig. 5.** Plain-view SEM image of a 200 nm-thick VO<sub>2</sub> sample after the grafting (a) Au and (b) Zr-containing NPs.

These features were further inspected at higher magnification by means of (S)TEM based techniques (**Fig. 6**). **Fig. 6(a–c)** summarizes the main results of such inspection in sample VO<sub>2</sub>/Au under TEM imaging conditions. **Fig. 6(a)** is a bright-field image (BFTEM) of the sample cross-section which allows to distinguish both the VO<sub>2</sub> thin film (with the intended thickness of about 200 nm) and the Au NPs as the dark spots all over the surface and marked with arrows. Observing them at higher magnification using high-resolution TEM (HRTEM, **Fig. 6(b)**), it appears that their actual size is slightly lower than the nominal one: About 20 nm instead of 30 nm. It is worth of noting that these NPs seem to be actually formed by smaller, nanoscopic grains with sizes below



about 10 nm. Moreover, it is shown that there are many lattice fringes randomly oriented with respect to each other. The measurement of some of these fringes leads to spacings which are quite similar, with values of about 2.35-2.40 Å. This distance is very close to that of the (111) lattice planes of gold ( $d_{0,hkl} = 2.356$  Å, taking into account for this calculation the values provided by SpringerMaterials database[59]), thus already confirming the chemical nature of these nanostructures. Their nanocrystalline character can be observed more clearly by retrieving the Fast Fourier Transform (FFT, **Fig. 6(c)**) of the region approximately within the red square of **Fig. 8(b)**. In this FFT, which shows the selected area in the reciprocal space, it is possible to distinguish some arcs whose distances to the center can be linked to the aforementioned (111) lattice planes in the real space. In addition, there is a small spot a bit farther away from the center of the FFT, which means that its associated lattice spacing in real space will be smaller. The resulting spacing is about 2 Å, which is similar to that of another plane of gold (i.e.,  $d_{0,200} = 2.040$  Å).

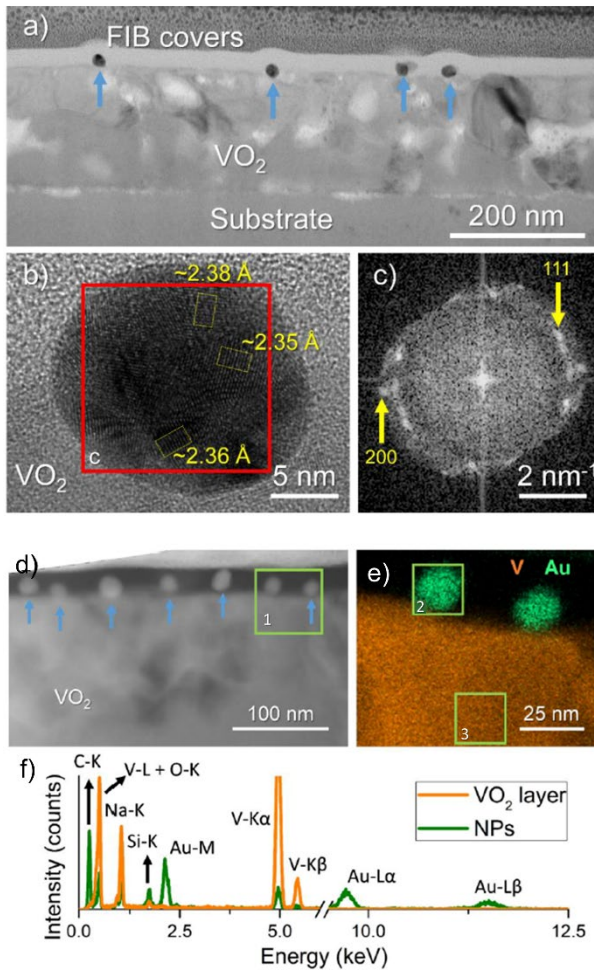


**Fig. 6.** For sample VO<sub>2</sub>/Au: (a) BFTEM cross-sectional micrograph; (b) HRTEM image zooming on one of the nanoparticles together with (c) its associated FFT indicating contributions by two lattice planes; (d) STEM-HAADF micrograph; (e) EDX net count map from a region identified in (d) as 1 showing contributions by vanadium and gold together with the (f) EDX spectra associated to 2 (green) and 3 (orange) regions highlighted in (e).

The NPs of these samples are subsequently studied by means of techniques more focused on gathering compositional information using STEM imaging conditions. Namely, we resorted to both high-angle annular dark field microscopy (STEM-HAADF) and energy-dispersive X-ray spectroscopy (EDX) and their main results on

the studies of these superficial NPs are summarized in **Fig. 6(d–f)**. In this sense, **Fig. 6(d)** is a STEM-HAADF micrograph that depicts several NPs distributed along the VO<sub>2</sub> surface. It is worth remarking here that, due to the physical phenomena involved in the formation of STEM-HAADF images, the intensity that results in these micrographs not only depends on the thickness of the sample, but it also mainly depends on the average atomic number of the material that is being scanned by the electron probe[60].

Since gold is about three times heavier than vanadium, the NPs are quite easy to identify, at least qualitatively in **Fig. 6(d)**. The chemical nature of these NPs is definitely confirmed by EDX, as **Fig. 6(e)** shows. This is an EDX map, extracted from the area 1 approximately marked in **Fig. 6(d)**, where the total net counts (i.e., the ones obtained after correcting the EDX spectrum generated at the mapped area) of only vanadium (orange) and gold (green) are considered. If EDX spectra from the regions marked in this map are extracted (**Fig. 6(f)**), X-ray peaks belonging to both elements can be found mainly in the regions of the sample where they were expected.

Nevertheless, peaks by other elements can be found, and their origins can be explained. Firstly, at about 270 eV, carbon originated by either electron probe contamination or the FIB process (we always used two covers for the surface to improve visibility of the NPs: one made out of carbon and another one above made out of platinum) is found. The V-L and O-K peaks have very similar energies, so they are unavoidably mixed at the same range. Both sodium and silicon (and also oxygen) originate from the glass substrate[61]. Note that the original spectrum was registered using an energy range of 20 keV, but it was not fully represented in the figure so as to make it easier to observe the peaks of interest. For the same reason, a part of the spectra from about 6 to about 10 keV has also been omitted. In this second range, there are some peaks caused by copper that are related to the redeposition of this metal as small particles at random positions of

the samples during the FIB preparation process (the support grids are made out of this element). Sometimes in the EDX analyses, small peaks belonging to Ar, which originate from the atmosphere within the growth chamber, could be found.

Thanks to the GAS method explained in section 2.3, it was also possible to deposit ZrN NPs on the VO<sub>2</sub> film as an alternative approach. The surface of sample VO<sub>2</sub>/ZrN after GAS deposition is shown in **Fig. 5(b)**. By comparing the coverage of Au and ZrN in their respective samples, it is possible to make two distinct observations. Firstly, the coverages (calculated using ImageJ software) are 5.2 and 3.2 % for samples VO<sub>2</sub>/ZrN and VO<sub>2</sub>/Au, respectively. Secondly, the GAS deposition results in a population of ZrN NPs with two different diameters of around 25 and 45 nm, estimated also using the same software. Compared to the results given by sample VO<sub>2</sub>/Au in this regard, it appears that this second surface has NPs of more heterogeneous sizes. The larger size is due to the agglomeration of smaller NPs, as already mentioned by Protsak et al.[32,40].

**Figure 7** depicts the (S)TEM studies conducted on sample VO<sub>2</sub>/ZrN. Again, the thickness of the VO<sub>2</sub> film is around the one intended, and the NPs are visible. In this sense, **Fig. 7(a)** proves the aforementioned hypothesis. That is, these NPs (areas marked with arrows) are more agglomerated compared to the behavior found in sample VO<sub>2</sub>/Au. They do not usually appear as individual structures, but rather as larger formations consisting of roughly sphere-shaped features that have sizes of about 10 and 20 nm. It seems reasonable to conclude that the size values given by the SEM measurements are slightly overestimated for both samples considering that the images used for those analyses were taken at lower magnification and thus have lower structural resolution to study such small features. However, unfortunately, although the HRTEM studies of this sample (not shown) indeed allow to confirm this size range as well as their nanocrystalline nature as happened with sample VO<sub>2</sub>/Au, none of the

regions found with measurable lattice fringes or columns seemed to contain any arrangement that could be reliably associated with any crystallographic projection belonging to cubic ZrN (using a lattice constant of  $a_0 = 4.68 \text{ \AA}$  as basis for calculations)[62]. Instead, depending on the area, isolated contributions by other Zr-containing nitrides (e.g.,  $\text{Zr}_4\text{N}_5$ )[63], oxides (e.g.,  $\text{ZrO}_2$ )[64] or even oxynitrides (e.g.,  $\text{Zr}_7\text{O}_8\text{N}_4$ )[65] could be identified as possible candidates. However, the authors of the present work consider that these HRTEM observations are highly speculative at the time being and not conclusive for three reasons. First of all, their results by HRTEM are very variable, and some areas did not even give any matches without assuming abnormally high errors in the measurements given the chosen image calibrations. Secondly, the literature on some of these compounds and their crystallographic data is scarce and/or unclear, making it difficult to make meaningful comparisons and decide whether or not the presence of some of these materials is realistic. Finally, according to other authors who used GAS to fabricate ZrN NPs[40,66], it is likely that the ZrN NPs are forming agglomerates of smaller particles, have irregular shapes, or form oxides or oxynitrides by exposure to the atmosphere. Although they only provided results on indirect observation techniques (e.g., X-ray photoelectron spectroscopy measurements) to support these claims, it appears that they partly agree with our findings, and it can be concluded at least that neither sample  $\text{VO}_2/\text{ZrN}$  (nor sample  $\text{VO}_2/\text{ZrN}/\text{VO}_2$ , presented later on) have only pure ZrN nanoparticles.

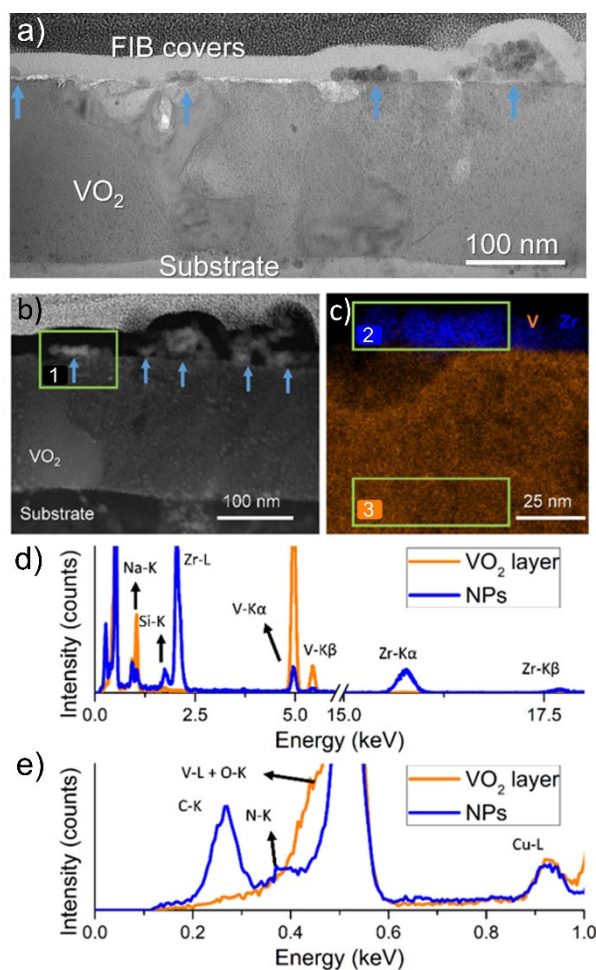


**Fig. 7.** For sample  $\text{VO}_2/\text{ZrN}$ : (a) BFTEM and (b) STEM-HAADF cross-sectional micrographs showing the whole layer; (c) EDX net count map from a region identified in (b) as 1 showing contributions by vanadium and zirconium; and (d-e) EDX spectra associated to regions 2 (blue) and 3 (orange) in (c) at different energy ranges.

As was done with sample  $\text{VO}_2/\text{Au}$ , this second system was explored using STEM-HAADF imaging as well as EDX. **Fig. 7(b–e)** is another summary of the findings related to the application of these techniques. In this case, since zirconium is a lighter element than gold, the Zr-containing NPs are generally closer in intensity to the one exhibited by the  $\text{VO}_2$  layer on observing them simultaneously by STEM-HAADF (**Fig. 7(b)**), although their agglomerated character eases their identification. The EDX net

counts map registered closer to one of the agglomerations (**Fig. 7(c)**, which is also approximately marked in the HAADF micrograph) and only selecting the net counts by vanadium (orange) and zirconium (blue) indeed confirms that those nanostructures are zirconium-rich. However, it is also necessary to check whether or not they contain nitrogen. Since this is a light element, its identification or even quantification by EDX can be very challenging[67] unless both counts are registered in any given EDX experiment and no peaks by other elements are nearby screening its signal. Fortunately, this was possible by retrieving an EDX spectrum from a large enough region of the NPs. The result is presented in **Fig. 7(d)** and **(e)**, which show spectra from both the VO<sub>2</sub> layer (orange) and the NPs (blue) at two different energy ranges: From 0 to about 18 keV and from 0 to 1 keV, respectively. While the same peaks previously described can be found in **Fig. 7(d)** (naturally minus those of Au, which is replaced by signals related to Zr), one can notice an additional, small shoulder originated from nitrogen at about 400 eV when the initial range of the spectrum is magnified (**Fig. 7(e)**). However, since this peak is so close to that related to the combination of V-L and O-K peaks, which come from the neighboring main material in this sample (i.e., the VO<sub>2</sub> layer underneath), it is screened very easily. But compared to the spectrum from the film, it is clear that there is a signal related to nitrogen only when the NPs are probed. Consequently, although it cannot be proved that there is only pure ZrN in this sample for the reasons previously given. It is possible to conclude that Zr-containing nanomaterial should be at least present together with oxygen and/or nitrogen.

The transmittance spectra of the VO<sub>2</sub>/NPs platform decorated with either Au or ZrN NPs, as a function of temperature are compared with those of bare VO<sub>2</sub> in **Fig. 8**. These graphs demonstrate the optical characteristics of infrared spectrum are affected by NPs grafting on the VO<sub>2</sub> film surface. There is an increase of 7% in infrared transmittance in

the cold state and a decrease of 5% in hot state. Moreover, infrared transmittance increases in the cold state and decreases in the hot state for NPs (Au or ZrN). As can be seen from **Fig. 8(b)**, there is a remarkable difference in amplitude of about 12%. This effect can be explained by an anti-reflection effect caused by NPs. Anti-reflection coatings reduce optical reflection by causing destructive interference at the interfaces, enhancing light transmittance. This minimizes reflection at the air/VO<sub>2</sub> interface, increasing the amount of light passing through the VO<sub>2</sub> layer and improving infrared light modulation during phase transition. A similar behavior has been demonstrated by Wang et al. while coupling SiO<sub>2</sub> NPs with VO<sub>2</sub>[68]. Slight variation in the anti-reflection effect when Zr-containing NPs are used instead of Au NPs is probably attributed to the lower NPs coverage on the surface, reducing the influence of NPs.

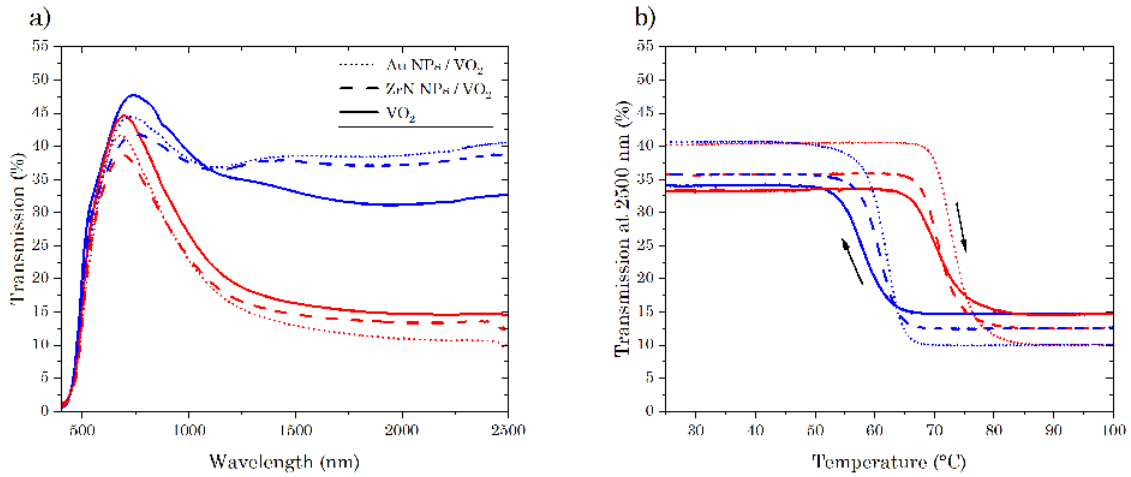


**Fig. 8.** (a) Transmittance spectra and (b) thermal hysteresis loop at 2500 nm of 200 nm thick VO<sub>2</sub> film coupled with Au NPs (dotted line) or ZrN NPs (dashed line). Data for bare VO<sub>2</sub> film of identical thickness is also reported (solid line). For (a), the colors correspond to the temperature: 25 °C is blue and 100 °C is red. For (b), red and blue represent the increase and decrease in temperature, respectively.



The corresponding hysteresis parameters are compiled in **Table 1**. In addition to the hysteresis amplitude enhancement discussed in the previous paragraph, the critical temperatures as well as the hysteresis width are slightly impacted by the presence of NPs. Grain size, lattice distortion, and compressive strain are the variables that can generally modify the phase transition temperature of VO<sub>2</sub> film. In our case, the grain size is unchanged by the presence of NPs because they are grafted after the VO<sub>2</sub> crystallization. We suppose that this variation is not due to some lattice distortions caused by the lattice mismatch between metallic NPs in contact with VO<sub>2</sub> film. Another reason can be the possible oxidation of the extreme VO<sub>2</sub> surface, as detected by Raman measurements, and defect incorporation as a result of the chemical protocol of NPs grafting or the ZrN deposition.

**Table 1.** Hysteresis parameters obtained from optical transmittance measurements of VO<sub>2</sub> thin film coupled with Au or ZrN NPs and for bare VO<sub>2</sub> film.

Sample	Critical Temperature (°C)			Width (°C)	Amplitude @ 2500 nm(%)
	Heating	Cooling	Average		
VO <sub>2</sub>	70.0	57.4	63.7	12.6	18.4
ZrN NPs/VO <sub>2</sub>	71.0	59.7	65.3	11.3	23.0
Au NPs/VO <sub>2</sub>	72.7	62.2	67.4	10.5	30.1

As with the optical properties, the resistivity is modified in the presence of NPs. **Fig.-9** shows the electrical resistivity for the bare VO<sub>2</sub> and for samples where the NPs are grafted onto the surface. It can be noticed that at low temperature the ZrN NPs have no, or slight, influence on the VO<sub>2</sub> resistivity. This result can be understood by the fact that the ZrN NPs have their surface oxidized, and, they cannot effectively contribute to reducing the resistivity by providing electrons or facilitating their transport. Moreover, at high temperatures, when VO<sub>2</sub> becomes metallic, the presence of Au NPs on the

surface provides additional electrons and conductive paths for electrons, reducing the overall resistivity of the system. ZrN NPs, being semiconducting, they do not reduce resistivity as effectively as the Au NPs. Thanks to the resistivity increase at low temperature and decrease at high temperature generated by the grafting of Au NPs onto VO<sub>2</sub>, the amplitude of the hysteresis is higher for this platform than for bare VO<sub>2</sub>.

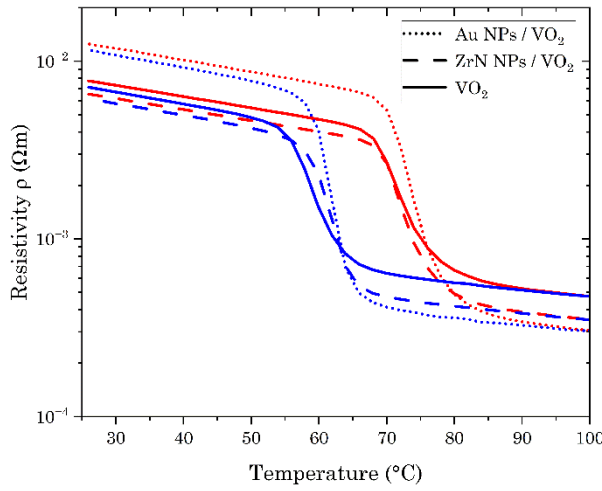


**Fig. 9.** Temperature dependence of the resistivity for 200 nm thick VO<sub>2</sub> film coupled with Au NPs (dotted line) or ZrN NPs (dashed line) and 200 nm thick bare VO<sub>2</sub> layer (solid line).

The surface roughness of the samples, detailed in **Table 2**, was measured from the topography images acquired during the initial AFM experiment conducted at the lowest temperature, as seen in **Fig. 10**. Among the samples, the VO<sub>2</sub> film exhibited the lowest roughness. In contrast, the samples containing NPs showed significantly higher roughness. Au NPs appeared mostly spherical, with diameters ranging between 10 and 20 nm. On the other hand, ZrN NPs were larger and more irregular in both shape and size. While the images were taken from regions of the sample densely populated with

NPs, it is important to highlight that other regions displayed far fewer nanoparticles. This variability in NP distribution across the surface could contribute to the differences in surface roughness observed across various areas of the samples.

**Table 2.** Roughness values of different samples.

Sample	RMS Roughness ( $S_q$ , nm)	Mean Roughness ( $S_a$ , nm)
VO <sub>2</sub>	4.1	3.2
ZrN NPs/VO <sub>2</sub>	6.0	4.5
Au NPs/VO <sub>2</sub>	5.3	3.9

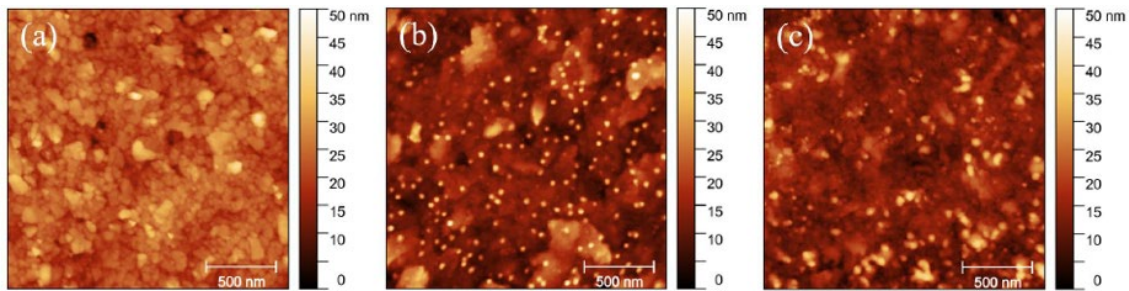


**Fig. 10.** AFM topographic images of the three samples: (a) VO<sub>2</sub>, (b) VO<sub>2</sub>/Au NPs, and (c) VO<sub>2</sub>/ZrN NPs.

### 3.3. Study of VO<sub>2</sub>/NPs/VO<sub>2</sub> hybrid thin films

**Fig. 11** compiles several images illustrating that both Au NPs and ZrN NP-based hybrid structures (i.e., using either type of NPs) were fabricated successfully. In this sense, the NPs are located at about halfway inside the VO<sub>2</sub> layer (i.e., 100 nm from the substrate and 100 nm away from the surface) and are characterized by the same shapes and coverage as when they were placed on the surface of the films. This means that under

BFTEM imaging conditions, Au NPs look again like large, dark particles (**Fig. 11(a)**, features marked with arrows), which become noticeably bright by HAADF (**Fig. 11(c)**) thanks to the difference in atomic number compared to that of vanadium. The resulting EDX net count map of this same micrograph (**Fig. 11(d)**) definitely confirms the nature of these Au-NPs again (EDX spectra are not shown since they show the expected Au peaks). Accordingly, when ZrN-NPs are inserted, the same agglomerations of smaller particles appear again in the middle of the layers (**Fig. 11(b)**) exhibiting the same subtle increased HAADF intensity as before (**Fig. 11(e)**). The presence of zirconium in this sample is confirmed once more by EDX mapping experiments carried out along this layer (**Fig. 11(f)**), but unfortunately, ambiguities comparable to the ones previously reported regarding their actual composition remain here after studying several HRTEM micrographs taken along this interface. Consequently, it is not possible to conclude that there is only pure ZrN in this region of the sample but rather a mixture of Zr-N-O compounds.

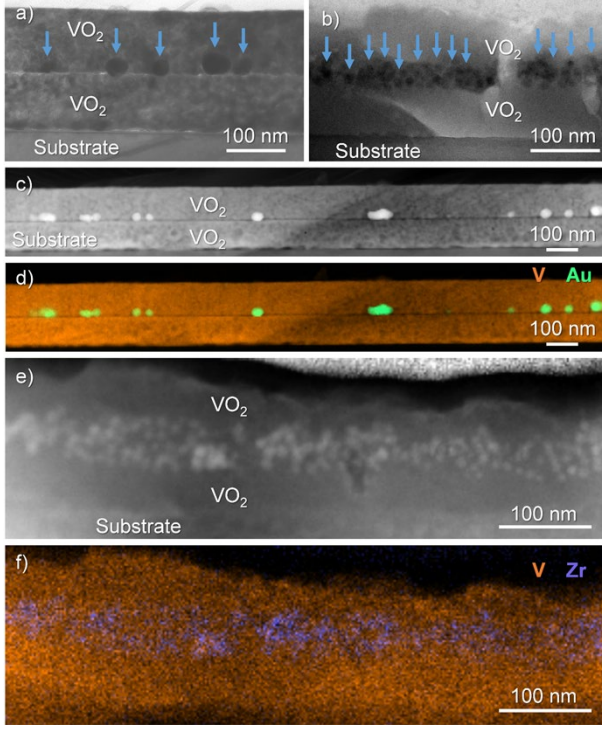


**Fig. 11.** (a, b) BFTEM cross-sectional micrographs and (c, e) HAADF images and their respective (d, f) EDX net counts maps of VO<sub>2</sub>/Au/VO<sub>2</sub> and VO<sub>2</sub>/ZrN/VO<sub>2</sub>, respectively.

As for the NPs/VO<sub>2</sub> platforms, the evolution of optical properties as a function of temperature is first measured (**Fig. 12**) to obtain the MIT parameters (see **Table 3**). Firstly, the ZrN NP sample exhibits the same anti-reflection behavior that was previously noted when the NPs are grafted on the VO<sub>2</sub> film surface. For VO<sub>2</sub> film and VO<sub>2</sub>/ZrN/VO<sub>2</sub>, the hysteresis parameter  $T_{MIT}$  values are 63.7 °C and 65.5 °C, respectively. Here also, the hysteresis width is reduced and reaches 9 °C, which is remarkably low compared to NPs/VO<sub>2</sub> platforms. In contrast to the latter samples, the VO<sub>2</sub> is now annealed, and crystallized when the ZrN NPs are already inserted inside the film. We suppose that this approach will disturb the crystalline quality of the upper VO<sub>2</sub> layer and then, create a lattice strain, which can reduce the hysteresis width and increase the  $T_{MIT}$ [69].

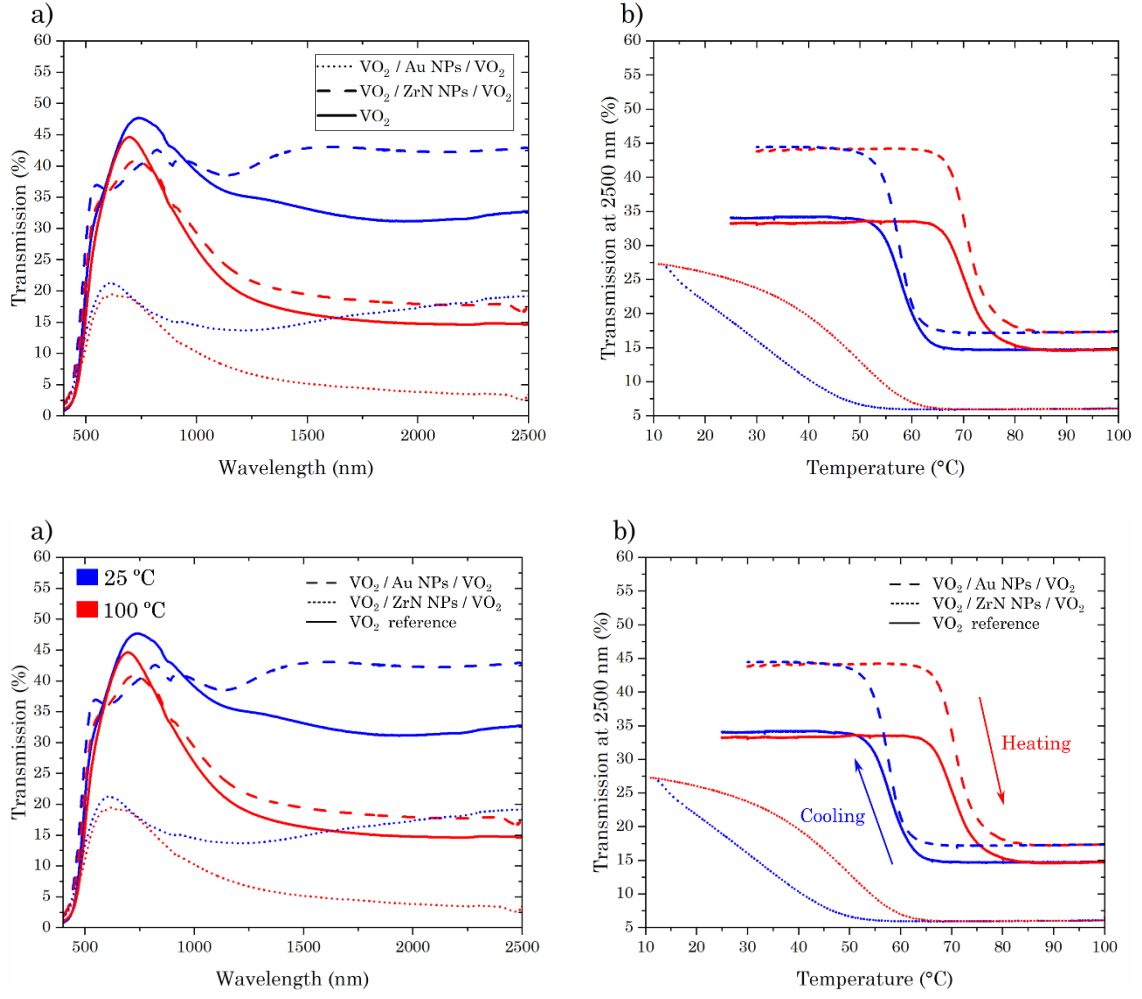


**Fig. 12.** (a) Transmittance spectra and (b) thermal hysteresis loop at 2500 nm for 200 nm thick VO<sub>2</sub>/NP/VO<sub>2</sub> platforms when the NPs are Au (dotted line) or ZrN (dashed line). Data for bare VO<sub>2</sub> film of identical thickness is also reported (solid line). For (a), the colors correspond to the temperature: 25 °C is blue and 100 °C is red. For (b), red and blue represent the increase and decrease in temperature, respectively.

On the other hand, the platform fabricated with Au NPs behaves differently, giving a lower transmittance and a lower gap between the cold and hot states. Additionally, the  $T_{MIT}$ , is found to be significantly lowered to a value close to room temperature. This

performance can be attributed to an electron doping effect originating from the incorporation of the Au NPs. Doping increases the electron density in the film, causing a shift in the Fermi energy level towards the conduction band. The introduction of donors inevitably leads to a decrease in optical transmittance and also in resistivity, as measured in the next section. When the VO<sub>2</sub> is in contact with Au NPs, a Schottky junction is formed, leading to the reconstruction of energy band structures. The work functions of pure VO<sub>2</sub> and Au are estimated at 5 eV and 3.7 eV, respectively. The Fermi levels of the two materials align and create an electron flow from the NPs to the VO<sub>2</sub>. This will increase the electron density in the matrix of VO<sub>2</sub>, which is considered like n-type doping. This doping reduces the Coulomb energy barrier, and the temperature required for the phase transition decreases. The same phenomenon has been described by Jian et al.[70], creating a VO<sub>2</sub>-Au NPs nanocomposite, and also with other metals such as W, Mo or Nb[71] or using co-doping with Ti-W[72] or F-W for example[73]. In particular, the VO<sub>2</sub>/Au/VO<sub>2</sub> system shows a smoother transition and a substantial reduction in transition temperature, consistent with electron-doping effects. The VO<sub>2</sub>/ZrN/VO<sub>2</sub> structure exhibits a more pronounced modulation amplitude and a slightly narrower hysteresis, while its transition temperature remains close to that of pristine VO<sub>2</sub>. These behaviors are attributed to distinct interfacial mechanisms, without evidence of a change in the fundamental nature of the phase transition. Also, the platform with NPs inside has a greater interfacial contact between VO<sub>2</sub> and Au NPs compared to the Au NPs/VO<sub>2</sub>, which could explain why we see this  $T_{MIT}$  reduction only here. Interestingly, this phenomenon occurs only for Au and not for ZrN NPs because, as highlighted by the team of Choukourov thanks to XPS analysis, ZrN NPs deposited by GAS technology might be oxidized, even partially, thus giving semiconducting

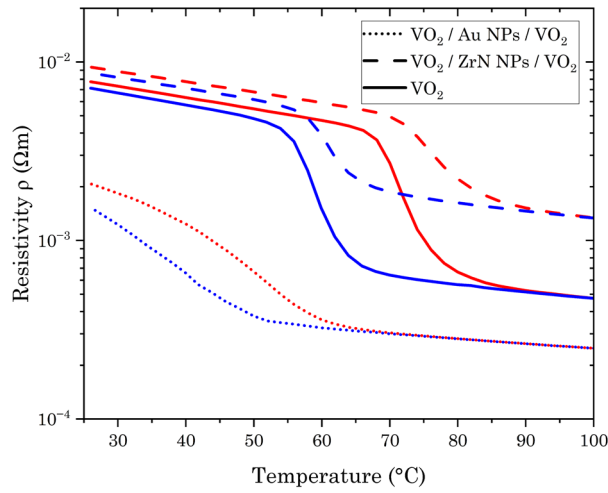
instead of metallic NPs[66]. The oxidized shell likely prevents electron transfer from the NPs to the VO<sub>2</sub> layer.

**Table 3.** Hysteresis parameters of platforms made of Au or ZrN NPs inside VO<sub>2</sub> layers (200 nm total thickness). Bare VO<sub>2</sub> film is also reported as reference.

Sample	Critical Temperature (°C)			Width (°C)	Amplitude @ 2500 nm(%)
	Heating	Cooling	Average		
VO <sub>2</sub>	70.0	57.4	63.7	12.6	18.4
VO <sub>2</sub> / ZrN NPs / VO <sub>2</sub>	70.3	61.2	65.5	9.1	27.1
VO <sub>2</sub> / Au NPs / VO <sub>2</sub>	41.2	29.2	35.5	12.0	22.5

Sheet resistivity measurements were also carried out in order to discuss the impact of the NPs on the electrical behavior. From **Fig. 13**, it can be observed that when the Au NPs are inside the VO<sub>2</sub> matrix, in addition to reducing the critical temperature  $T_{MIT}$ , the Au NPs presence reduces the global resistivity even at low and high temperatures. As discussed earlier, this phenomenon is explained by the electron doping of the VO<sub>2</sub> layer, which will obviously reduce the resistivity. But for ZrN NPs, as they are semiconducting, their presence in the VO<sub>2</sub> layer decreases the concentration of the charge carriers, which leads to an increase in resistivity.

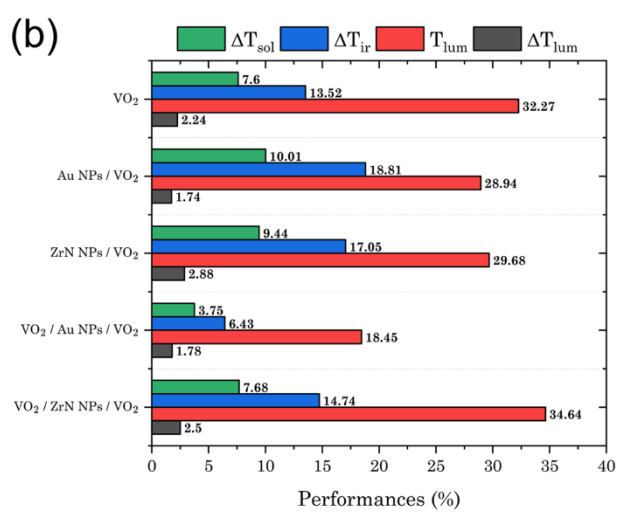
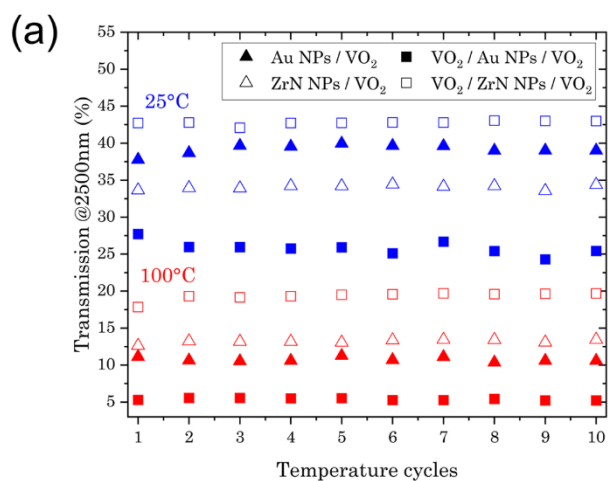




**Fig. 13.** Temperature dependence of the resistivity for a 200 nm thick VO<sub>2</sub>/NP/VO<sub>2</sub> platforms when NPs are Au (dotted line) or ZrN (dashed line). Resistivity of 200 nm thick bare VO<sub>2</sub> is also shown (solid line).

### 3.4 Stability and Light Modulation Performance

Optical transmittance of all the VO<sub>2</sub>-based samples measurements at a wavelength of 2500 nm for temperature cycles provide a relevant appraisal of the stability of the materials. For this purpose, the temperature increases from 25°C to 100°C. Then, it comes back to the starting value of 25°C. This cycle is repeated 10 times. Every sample previously characterized is submitted to this test (**Fig. 14(a)**). Apart from some slight variations due to the experimental manipulation, temperature stability is demonstrated for each sample. Such stability is an important issue for many applications where it must be constant over time after many uses.



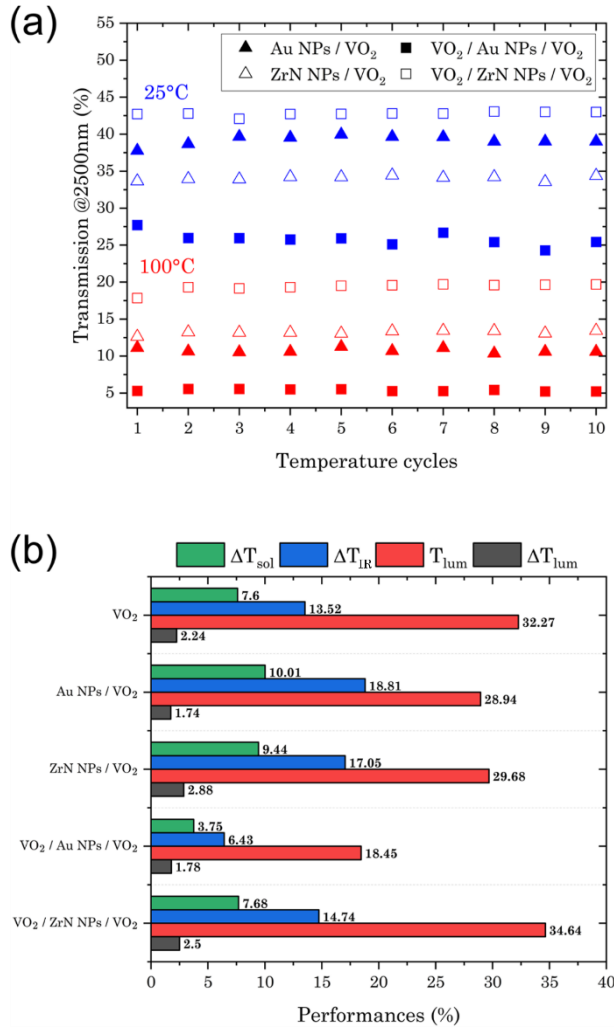


**Fig. 14.** (a) Transmittance measured at 2500 nm, during 10 successive temperature cycles, for all platforms. (b) Values of  $\Delta T_{sol}$  (green),  $\Delta T_{IR}$  (blue),  $T_{lum}$  (red) and  $\Delta T_{lum}$  (dark) for each platform.

VO<sub>2</sub>-based coatings are candidates for smart, energy-saving, windows. In this respect, the energy modulation efficiency is a crucial aspect. Optical performance is primarily characterized by parameters such as light transmittance ( $T_{lum}$  in **Eq. 4**) and solar energy modulation ( $\Delta T_{sol}$  in **Eq. 1**). Solar transmittance,  $T_{sol}$  (**Eq. 2**), quantifies the amount of solar energy that passes through a film. This measurement plays a role in the frame of the solar modulation efficiency. Solar modulation,  $\Delta T_{sol}$ , is derived from the difference

in solar transmittance between hot and cold states and essentially represents the solar energy blocked by the thermochromic coating, which varies according to the ambient temperature. It is calculated as follows according to **Eq. 1**:

$$\Delta T_{sol} = T_{sol,100^\circ C} - T_{sol,25^\circ C} \quad (1)$$

$$T_{sol} = \frac{\int_{280}^{2500} T(\lambda) \phi_{sol}(\lambda) d\lambda}{\int_{280}^{2500} \phi_{sol}(\lambda)} \quad (2)$$

Where  $T(\lambda)$  is the transmittance at each wavelength value and  $\phi_{sol}(\lambda)$  is the solar radiation spectrum at sea level.

Luminous transmittance,  $T_{lum}$ , is the  $V(\lambda)$ -weighted visible light transmission (380–780 nm) through a material, which quantifies visual transparency. To measure it, we use the transmittance,  $T(\lambda)$ , and the luminous sensitivity of the human eye,  $\phi_{lum}$ , obtained from the CIE (Commission Internationale de l'Éclairage). The variation of  $T_{lum}$  between hot and cold states, called  $\Delta T_{lum}$ , can be calculated, but it would be negligible since the transmittance in the visible range changes weakly with temperature (see **Fig. 3(a)**). Therefore, only the value of  $T_{lum}$  at 25 °C is given. Its expressions are defined in **Eq. 4**:

$$\Delta T_{lum} = T_{lum,100^\circ C} - T_{lum,25^\circ C} \quad (3)$$

$$T_{lum} = \frac{\int_{380}^{780} T(\lambda) \phi_{lum}(\lambda) d\lambda}{\int_{380}^{780} \phi_{lum}(\lambda)} \quad (4)$$

However, an additional integral quantity can be calculated: The infrared transmittance,  $T_{IR}$ , which has a similar definition to  $T_{sol}$ , but with a smaller integration range from 780 nm to 2500 nm:

$$T_{IR} = \frac{\int_{780}^{2500} T(\lambda) \phi_{sol}(\lambda) d\lambda}{\int_{780}^{2500} \phi_{sol}(\lambda)} \quad (5)$$

$$\Delta T_{IR} = T_{IR,100^\circ C} - T_{IR,25^\circ C} \quad (6)$$

This parameter quantifies the amount of infrared radiation transmitted, which mainly affects the temperature inside buildings. Furthermore, we have previously observed in **Fig. 3(a)** that the optical transmittance in this wavelength range varies enormously with temperature for VO<sub>2</sub> thin films.

These four parameters (i.e.,  $\Delta T_{IR}$ ,  $\Delta T_{sol}$ ,  $\Delta T_{lum}$  and  $T_{lum}$ ) allow to study the modulation performance over the relevant light spectrum and the transparency of the material (with  $T_{lum}$ ) and are all reported in **Fig. 14(b)**. Firstly, we observe that for VO<sub>2</sub> platforms with NPs grafted on the surface, the light modulation is improved thanks to the enhanced scattering effect created by the NPs layer, as explained in section 3.2. As a result,  $\Delta T_{sol}$  goes from 7.6% to 10% with Au NPs and up to 9.4% with ZrN NPs. Regarding  $\Delta T_{IR}$ , it reaches 18.8% and 17% for Au and ZrN NPs coupling, respectively, while bare VO<sub>2</sub> gives 13.5%. However, when the Au NPs are incorporated inside the VO<sub>2</sub> layer, these parameters decrease due to the NPs electronic doping effect reducing the transmittance spectra. For ZrN NPs,  $\Delta T_{sol}$  and  $\Delta T_{IR}$  remain almost unchanged, although in **Fig. 12** the gap between the cold and hot states is larger, which would imply an increase in  $\Delta T_{sol}$  and  $\Delta T_{IR}$ . Unfortunately, this effect is offset by the presence of a dip between 500 nm and 900 nm, certainly caused by a plasmonic absorption band. This range has a significant impact on the performance, because the radiation spectra are at their maximum. In terms of transparency, expressed by  $T_{lum}$  and  $\Delta T_{lum}$ , **Fig. 14(b)** shows, as expected for VO<sub>2</sub> films, a low  $\Delta T_{lum}$  performance. There is also a slight decrease in  $T_{lum}$  for all platforms due to the decrease in transmittance in the visible range caused by the plasmonic absorption of the NPs.

By comparing all those results, two platforms can be considered as the most promising candidates for smart windows applications. Indeed, for NPs/VO<sub>2</sub> samples, either with ZrN or Au,  $\Delta T_{sol}$  and  $\Delta T_{IR}$  are both enhanced compared to bare VO<sub>2</sub>. These two

parameters are the most important for this solar modulation application. Regarding  $T_{lum}$  and  $\Delta T_{lum}$ , no significant improvements are revealed for VO<sub>2</sub> films decorated by NPs on the surface. For VO<sub>2</sub>/NPs/VO<sub>2</sub> platforms, all parameters, except  $\Delta T_{sol}$ , are slightly improved when ZrN is incorporated. In contrast, when Au NPs are inside the layer, all parameters decrease due to the transmittance degradation. Overall, it should also be noted that, with the sole exception of what was reported for the VO<sub>2</sub>/Au NPs/VO<sub>2</sub> sample, the results of this study are consistent with recent state-of-the-art in this field. In this connection, the most recent scientific literature on VO<sub>2</sub> single layer films without complex antireflective coatings or excessive doping (beyond what is needed for  $T_c$  adjustment) establishes that  $T_{lum}$  and  $\Delta T_{sol}$  values typically range from 30–50% and 5–15%, respectively [74–77].

Beyond smart window applications, the VO<sub>2</sub>/NP composite architectures investigated in this work may also find relevance in other domains where thermally tunable optical properties are essential. Recent work by Alonzo-Zapata *et al.* [78] demonstrated that VO<sub>2</sub> thin films exhibit significant emissivity modulation across the phase transition, enabling the design of radiative thermal diodes and transistors. The integration of plasmonic nanoparticles in such systems could further enhance their tunability, opening avenues in dynamic thermal emissivity control, or other application like plasmon-assisted photonic switching, optical limiting, and gas sensing. These perspectives suggest that VO<sub>2</sub>/NP hybrid platforms can serve as multifunctional components for advanced thermal and optoelectronic applications.

#### **4. Conclusions**

This study investigated the evolution of the optoelectrical properties of materials elaborated by coupling thermochromic VO<sub>2</sub> thin films and NPs, specifically Au and

ZrN. Different configurations were chosen depending on the position of the NPs: With NPs deposited on the VO<sub>2</sub> surface or embedded inside two VO<sub>2</sub> layers.

The grafting of Au and ZrN NPs onto the surface of VO<sub>2</sub> thin films resulted in significant improvements in infrared light modulation. This improvement is attributed to the scattering effects induced by the NPs layer, particularly pronounced for Au NPs, leading to a substantial increase in the hysteresis amplitude. In contrast, embedding Au NPs within the VO<sub>2</sub> layer resulted in a significant decrease in transition temperature  $T_{MIT}$  which comes close to room temperature (35°C). This was attributed to an electron doping effect induced by the presence of Au NPs. On the other hand, the VO<sub>2</sub>/NP/VO<sub>2</sub> platform exhibited similar hysteresis characteristics to those recorded when NPs are located on the surface, suggesting their potential to enhance light modulation without significantly affecting the  $T_{MIT}$ . The observation of these samples by transmission electron microscopy techniques confirmed the presence of nanocrystalline gold particles distributed all over the VO<sub>2</sub> layers, either at the surface or in the middle of the films, depending on the sample. On the other hand, the current analyses of the ZrN NPs in their respective samples revealed a more agglomerated character of the particles, which also have a generally smaller size. Moreover, their comprehensive characterization led to conclude that they are more likely not just pure ZrN, but rather a mixture of different nitrides, oxides and even oxynitrides compounds.

The preliminary stability tests showed consistent performance over multiple temperature cycles, suggesting a significant potential for the implementation of these composite platforms in practical applications. Furthermore, the detailed analyses of optical parameters such as solar energy modulation ( $\Delta T_{sol}$ ), infrared transmittance ( $\Delta T_{IR}$ ) and light transmittance ( $T_{lum}$ ) provided valuable information on the overall performance of these materials for smart window applications. This work provides the

first comprehensive demonstration of how nanoparticle type and placement within VO<sub>2</sub> films can be leveraged to tailor both optical modulation and transition temperature, opening new pathways for functional thermochromic devices.

## **Acknowledgements**

S. Konstantinidis is Research Director of the National Funds for Scientific Research (FRS-FNRS Belgium). G. Savorianakis acknowledges the FRS-FNRS for financial support (FRIA grant). A. J. Santos, J. J. Jimenez and F. M. Morales wish to acknowledge the support given by the Spanish State Agency of Research through the national “Retos” projects call (references PID2020–114418RBI00 and PID2023-150975OB-I00). A. J. Santos would like to thank the University of Cádiz and the Spanish Ministerio de Universidades for the concession of a “Margarita Salas” postdoctoral fellowship funded by the European Union - NextGenerationEU (2021-067#9663/PN/MS-RECUAL/CD). M.D. also acknowledges the financial support from the Spanish Ministerio de Ciencia Innovación, under the project reference EQC 2018-004704-P FEDER 2014-2020.

## **Data availability statement**

Data will be made available on request.

## **Declaration of Competing Interest**

The authors declare that they have no known competing financial interests or personal relationships that could have appeared to influence the work reported in this paper.



## REFERENCES

- [1] M. Currie, V.D. Wheeler, B. Downey, N. Nepal, S.B. Qadri, J.A. Wollmershauser, J. Avila, L. Nyakiti, Asymmetric hysteresis in vanadium dioxide thin films, *Opt. Mater. Express*. 9 (2019) 3717. doi:10.1364/ome.9.003717.
- [2] V.A. Klimov, I.O. Timofeeva, S.D. Khanin, E.B. Shadrin, A. V. Ilinskii, F. Silva-Andrade, Hysteresis loop construction for the metal-semiconductor phase transition in vanadium dioxide films, *Tech. Phys.* 47 (2002) 1134–1139. doi:10.1134/1.1508078.
- [3] D. Brassard, S. Fourmaux, M. Jean-Jacques, J.C. Kieffer, M.A. El Khakani, Grain size effect on the semiconductor-metal phase transition characteristics of magnetron-sputtered VO<sub>2</sub> thin films, *Appl. Phys. Lett.* 87 (2005) 38–41. doi:10.1063/1.2001139.
- [4] N. Shen, S. Chen, R. Huang, J. Huang, J. Li, R. Shi, S. Niu, A. Amini, C. Cheng, Vanadium dioxide for thermochromic smart windows in ambient conditions, *Mater. Today Energy*. 21 (2021) 100827. doi:10.1016/j.mtener.2021.100827.
- [5] J. Sang, W. Zhu, Y. Feng, Y. Liu, J. Shang, J. Sun, L. Guo, Y. Zhang, S. Zhao, V. Chigrinov, D.S. Seo, Smart Windows with a VO<sub>2</sub> Thin Film as a Conductive Layer for Efficient and Independent Dual-Band Modulation, *ACS Appl. Electron. Mater.* 3 (2021) 4882–4890. doi:10.1021/acsaelm.1c00728.
- [6] Y.E. Monfared, B.L. Kurylyk, M. Dasog, Highly Sensitive Plasmonic Fiber-Optic Sensors using Group IV Transition Metal Nitrides: a Numerical Investigation, *Plasmonics*. 17 (2022) 931–940. doi:10.1007/s11468-021-01579-3.

- [7] M. Kaufman, J. Vlček, J. Houška, S. Farrukh, S. Haviar, Design and Scalable Synthesis of Thermochromic VO<sub>2</sub>-Based Coatings for Energy-Saving Smart Windows with Exceptional Optical Performance, *ACS Appl. Mater. Interfaces*. 16 (2024) 57268–57276. doi:10.1021/acsami.4c05696.
- [8] I. Olivares, L. Sánchez, J. Parra, R. Larrea, A. Griol, M. Menghini, P. Homm, L.-W. Jang, B. van Bilzen, J.W. Seo, J.-P. Locquet, P. Sanchis, Optical switching in hybrid VO<sub>2</sub> /Si waveguides thermally triggered by lateral microheaters , *Opt. Express*. 26 (2018) 12387. doi:10.1364/oe.26.012387.
- [9] P. Markov, R.E. Marvel, H.J. Conley, K.J. Miller, R.F. Haglund, S.M. Weiss, Optically Monitored Electrical Switching in VO<sub>2</sub>, *ACS Photonics*. 2 (2015) 1175–1182. doi:10.1021/acsp Photonics.5b00244.
- [10] S. Chen, X. Yi, H. Ma, T. Xiong, H. Wang, C. Ke, Phase transition VO<sub>2</sub> thin films for optical switches, *Int. J. Infrared Millimeter Waves*. 25 (2004) 157–163. doi:10.1023/B:IJIM.0000012771.09884.61.
- [11] Z. Xu, G. Qin, A.A. Bernussi, Z. Fan, Electrothermally control of dynamic infrared switching of VO<sub>2</sub> thin film on FTO glass, *J. Alloys Compd*. 858 (2021) 157640. doi:10.1016/j.jallcom.2020.157640.
- [12] S. Chen, H. Ma, X. Yi, T. Xiong, H. Wang, C. Ke, Smart VO<sub>2</sub> thin film for protection of sensitive infrared detectors from strong laser radiation, *Sensors Actuators, A Phys*. 115 (2004) 28–31. doi:10.1016/j.sna.2004.03.018.
- [13] Y. Bu, J. Zou, Y. Liu, Z. Zhu, W. Deng, X. Peng, B. Tang, Simple and efficient synthesis of high-quality VO<sub>2</sub> thin films and their application in vacuum sensor with wide pressure range, *Thin Solid Films*. 638 (2017) 420–425. doi:10.1016/j.tsf.2017.08.013.

- [14] V.X. Hien, T.M. Thang, V.T. Dong, D.D. Nhat, N.T. Nghi, L.H. Phuoc, C.T. Khoa, D.D. Vuong, N.D. Chien, Synthesis of VO<sub>2</sub> thin films from vanadium powder and determination of room-temperature NH<sub>3</sub> sensing properties, *J. Mater. Sci. Mater. Electron.* 32 (2021) 13803–13812. doi:10.1007/s10854-021-05956-w.
- [15] A. Christensen, A.B. Posadas, B. Zutter, P. Finnegan, S. Bhullar, S. Bishop, A.A. Talin, A.A. Demkov, Effect of substrate and growth method on vanadium dioxide thin films by RF magnetron sputtering: Vanadium metal oxidation vs reactive sputtering, *J. Appl. Phys.* 134 (2023) 015301. doi:10.1063/5.0150898.
- [16] N.A. Fleeer, K.E. Pelcher, K. Nieto, E.J. Braham, J. Zou, G.A. Horrocks, Y. Naoi, S.W. Depner, B.J. Schultz, J. Amano, D.G. Sellers, S. Banerjee, Elucidating the Crystallite Size Dependence of the Thermochromic Properties of Nanocomposite VO<sub>2</sub> Thin Films, *ACS Omega.* 3 (2018) 14280–14293. doi:10.1021/acsomega.8b02093.
- [17] H. Qu, Y. Guo, D. Zhang, B. Sun, L. Yan, Composition evolution and electrical properties of VO<sub>2</sub> thin films induced by annealing temperature, *J. Sol-Gel Sci. Technol.* 104 (2022) 138–146. doi:10.1007/s10971-022-05912-y.
- [18] Y. Bleu, F. Bourquard, V. Barnier, A.S. Loir, F. Garrelie, C. Donnet, Towards Room Temperature Phase Transition of W-Doped VO<sub>2</sub> Thin Films Deposited by Pulsed Laser Deposition: Thermochromic, Surface, and Structural Analysis, *Materials.* 16 (2023) 461. doi:10.3390/ma16010461.
- [19] E. Breckenfeld, H. Kim, K. Burgess, N. Charipar, S.F. Cheng, R. Stroud, A. Pique, Strain effects in epitaxial VO<sub>2</sub> thin films on columnar buffer-layer TiO<sub>2</sub>/Al<sub>2</sub>O<sub>3</sub> virtual substrates, *ACS Appl. Mater. Interfaces.* 9 (2017) 1577–1584. doi:10.1021/acsami.6b13112.

- [20] J. Houska, Significant dependence of the efficiency of energy-saving thermochromic VO<sub>2</sub> on slight changes of its properties in the visible due to strain and/or vacancies, *Sol. Energy*. 282 (2024) 112973.  
doi:10.1016/j.solener.2024.112973.
- [21] P. Jin, M. Tazawa, G. Xu, Reversible tuning of surface plasmon resonance of silver nanoparticles using a thermochromic matrix, *J. Appl. Phys.* 99 (2006) 97–100. doi:10.1063/1.2193336.
- [22] J.C. Orlianges, J. Leroy, A. Crunteanu, R. Mayet, P. Carles, C. Champeaux, Electrical and optical properties of vanadium dioxide containing gold nanoparticles deposited by pulsed laser deposition, *Appl. Phys. Lett.* 101 (2012) 133102. doi:10.1063/1.4754708.
- [23] M. Maaza, O. Nemraoui, C. Sella, A.C. Beye, P.O. Box, S. Africa, U. Pierre-, M. Curie, P. Vi, P. Cedex, Surface Plasmon Resonance Thermochromic Nanocomposites, *Gold Bull.* 38 (2005) 100–106. doi:10.1007/BF03215243.
- [24] Z. He, J. Jian, S. Misra, X. Gao, X. Wang, Z. Qi, B. Yang, D. Zhang, X. Zhang, H. Wang, Bidirectional tuning of phase transition properties in Pt : VO<sub>2</sub> nanocomposite thin films, *Nanoscale*. 12 (2020) 17886–17894.  
doi:10.1039/d0nr04008h.
- [25] B.M.H. Kryder, E.C. Gage, T.W. Mcdaniel, W.A. Challener, R.E. Rottmayer, G. Ju, Y. Hsia, M.F. Erden, Heat Assisted Magnetic Recording, *Proc. IEEE*. 96 (2008) 1810–1835. doi:10.1109/JPROC.2008.2004315.
- [26] P. Pleskunov, M. Protsak, Z. Krtouš, T. Košutová, M. Tosca, K. Biliak, V. Červenková, D. Nikitin, J. Hanuš, M. Cieslar, I. Gordeev, M. Dopita, M. Vorochta, J. Kousal, L. Martinu, A. Choukourov, Refractory Plasmonics of

- Reactively Sputtered Hafnium Nitride Nanoparticles: Pushing Limits, *Adv. Opt. Mater.* 12 (2024) 2302715. doi:10.1002/adom.202302715.
- [27] M. Lee, J.U. Kim, K.J. Lee, S. Ahn, Y.B. Shin, J. Shin, C.B. Park, Aluminum Nanoarrays for Plasmon-Enhanced Light Harvesting, *ACS Nano*. 9 (2015) 6206–6213. doi:10.1021/acsnano.5b01541.
- [28] W. Li, U. Guler, N. Kinsey, G. V. Naik, A. Boltasseva, J. Guan, V.M. Shalae, A. V. Kildishev, Refractory plasmonics with titanium nitride: Broadband, *Adv. Mater.* 26 (2014) 7959–7965. doi:10.1002/adma.201401874.
- [29] K. Biliak, M. Protsak, P. Pleskunov, D. Nikitin, J. Hanuš, S. Ali-Ogly, J. Šomvářsky, M. Tosca, M. Cieslar, T. Košutová, M. Dopita, F. Lopes Ferreira, A. Choukourov, Plasmonic TiN, ZrN, and HfN Nanofluids for Solar-to-Heat Conversion, *ACS Appl. Nano Mater.* 6 (2023) 21642–21651. doi:10.1021/acsanm.3c03662.
- [30] A. Lalis, G. Tessier, J. Plain, G. Baffou, Plasmonic efficiencies of nanoparticles made of metal nitrides (TiN, ZrN) compared with gold, *Sci. Rep.* 6 (2016) 38647. doi:10.1038/srep38647.
- [31] U. Guler, A. Boltasseva, V.M. Shalae, Refractory plasmonics, *Science*. 344 (2014) 263–264. doi:10.1126/science.1252722.
- [32] M. Protsak, V. Červenková, D. Nikitin, S. Ali-Ogly, Z. Krtous, K. Biliak, P. Pleskunov, M. Tosca, R. Katuta, H. Biederman, B. Baloukas, L. Martinu, L. Bajtosova, M. Cieslar, M. Dopita, A. Choukourov, Gas-Aggregated Core-Shell ZrN@SiN Nanoparticles with Enhanced Thermal Stability for Plasmonic Applications at High Temperatures, *ACS Appl. Nano Mater.* 8 (2025) 3092–3103. doi:10.1021/acsanm.4c06843.

- [33] U. Guler, V.M. Shalaev, A. Boltasseva, Nanoparticle plasmonics: Going practical with transition metal nitrides, *Mater. Today*. 18 (2015) 227–237.  
doi:10.1016/j.mattod.2014.10.039.
- [34] G. Savorianakis, C. Rousseau, A. Sergievskaya, G. Rosolen, M. Voué, B. Maes, S. Konstantinidis, Plasmonic Resonance Shifts in Gold Nanoparticles-Thermochromic VO<sub>2</sub> Thin Film Hybrid Platforms: A Joint Experimental and Numerical Study, *Adv. Mater. Interfaces*. 2400172 (2024) 2400172.  
doi:10.1002/admi.202400172.
- [35] J. Kimling, M. Maier, B. Okenve, V. Kotaidis, H. Ballot, A. Plech, Turkevich method for gold nanoparticle synthesis revisited, *J. Phys. Chem. B*. 110 (2006) 15700–15707. doi:10.1021/jp061667w.
- [36] D.F.S. Petri, G. Wenz, P. Schunk, T. Schimmel, An improved method for the assembly of amino-terminated monolayers on SiO<sub>2</sub> and the vapor deposition of gold layers, *Langmuir*. 15 (1999) 4520–4523. doi:10.1021/la981379u.
- [37] J.A. Howarter, J.P. Youngblood, Optimization of silica silanization by 3-aminopropyltriethoxysilane, *Langmuir*. 22 (2006) 11142–11147.  
doi:10.1021/la061240g.
- [38] P.Q.T. Do, V.T. Huong, N.T.T. Phuong, T.H. Nguyen, H.K.T. Ta, H. Ju, T.B. Phan, V.D. Phung, K.T.L. Trinh, N.H.T. Tran, The highly sensitive determination of serotonin by using gold nanoparticles (Au NPs) with a localized surface plasmon resonance (LSPR) absorption wavelength in the visible region, *RSC Adv*. 10 (2020) 30858–30869. doi:10.1039/d0ra05271j.
- [39] G. Rampelberg, B. De Schutter, W. Devulder, K. Martens, I. Radu, C. Detavernier, In situ X-ray diffraction study of the controlled oxidation and

- reduction in the V-O system for the synthesis of VO<sub>2</sub> and V<sub>2</sub>O<sub>3</sub> thin films, J. Mater. Chem. C. 3 (2015) 11357–11365. doi:10.1039/c5tc02553b.
- [40] M. Protsak, K. Biliak, D. Nikitin, P. Pleskunov, M. Tosca, S. Ali-Ogly, J. Hanuš, L. Hanyková, V. Červenková, A. Sergievskaya, S. Konstantinidis, D. Cornil, J. Cornil, M. Cieslar, T. Košutová, T. Popelář, L. Ondič, A. Choukourov, One-step synthesis of photoluminescent nanofluids by direct loading of reactively sputtered cubic ZrN nanoparticles into organic liquids, *Nanoscale*. 16 (2023) 2452–2465. doi:10.1039/d3nr03999d.
- [41] S.J. Klepeis, J.P. Benedict, R.M. Anderson, A Grinding/Polishing Tool for TEM Sample Preparation, *MRS Proc.* 115 (1987) 179–184. doi:10.1557/proc-115-179.
- [42] P.M. Voyles, J.L. Grazul, D.A. Muller, Imaging individual atoms inside crystals with ADF-STEM, *Ultramicroscopy*. 96 (2003) 251–273. doi:10.1016/S0304-3991(03)00092-5.
- [43] H.-W. Cha, M.-C. Kang, K. Shin, C.-W. Yang, Transmission Electron Microscopy Specimen Preparation of Delicate Materials Using Tripod Polisher, *Appl. Microsc.* 46 (2016) 110–115. doi:10.9729/am.2016.46.2.110.
- [44] A.J. Santos, B. Lacroix, F. Maudet, F. Paumier, S. Hurand, C. Dupeyrat, V.J. Gómez, D.L. Huffaker, T. Girardeau, R. García, F.M. Morales, Application of advanced (S)TEM methods for the study of nanostructured porous functional surfaces: A few working examples, *Mater. Charact.* 185 (2022) 111741. doi:10.1016/j.matchar.2022.111741.
- [45] F. Ureña-Begara, A. Crunteanu, J.P. Raskin, Raman and XPS characterization of vanadium oxide thin films with temperature, *Appl. Surf. Sci.* 403 (2017) 717–727. doi:10.1016/j.apsusc.2017.01.160.

- [46] V.M. Dzhagan, M.Y. Valakh, O.F. Isaieva, V.O. Yukhymchuk, O.A. Stadnik, O.Y. Gudymenko, P.M. Lytvyn, O.A. Kulbachynskyi, V.S. Yefanov, B.M. Romanyuk, V.P. Melnik, Raman fingerprints of different vanadium oxides as impurity phases in VO<sub>2</sub> films, *Opt. Mater. (Amst)*. 148 (2024) 114894. doi:10.1016/j.optmat.2024.114894.
- [47] K.D. Rogers, An X-ray diffraction study of semiconductor and metallic vanadium dioxide, *Powder Diffr.* 8 (1993) 240–244. doi:10.1017/S0885715600019448.
- [48] A.J. Santos, N. Martin, J. Outón, E. Blanco, R. García, F.M. Morales, A simple two-step approach to the fabrication of VO<sub>2</sub>-based coatings with unique thermochromic features for energy-efficient smart glazing, *Energy Build.* 285 (2023) 112892. doi:10.1016/j.enbuild.2023.112892.
- [49] H. Zhang, Z. Wu, C. Wang, Y. Sun, VO<sub>2</sub> film with small hysteresis width and low transition temperature, *Vacuum*. 170 (2019) 108971. doi:10.1016/j.vacuum.2019.108971.
- [50] D.P. Zhang, M.D. Zhu, Y. Liu, K. Yang, G.X. Liang, Z.H. Zheng, X.M. Cai, P. Fan, High performance VO<sub>2</sub> thin films growth by DC magnetron sputtering at low temperature for smart energy efficient window application, *J. Alloys Compd.* 659 (2016) 198–202. doi:10.1016/j.jallcom.2015.11.047.
- [51] S. Chen, H. Zhang, High visible transmittance of VO<sub>2</sub> film prepared by DC magnetron sputtering with situ annealing, *J. Opt.* 50 (2021) 508–511. doi:10.1007/s12596-021-00719-6.
- [52] X. Chen, Q. Lv, Resistance hysteresis loop characteristic analysis of VO<sub>2</sub> thin film for high sensitive microbolometer, *Optik (Stuttg)*. 126 (2015) 2718–2722.



doi:10.1016/j.ijleo.2015.06.076.

- [53] D.H. Jung, H.S. So, K.H. Ko, J.W. Park, H. Lee, T.T.T. Nguyen, S. Yoon, Electrical and optical properties of VO<sub>2</sub> thin films grown on various sapphire substrates by using RF sputtering deposition, J. Korean Phys. Soc. 69 (2016) 1787–1797. doi:10.3938/jkps.69.1787.
- [54] D. Ruzmetov, D. Heiman, B.B. Claflin, V. Narayanamurti, S. Ramanathan, Hall carrier density and magnetoresistance measurements in thin-film vanadium dioxide across the metal-insulator transition, Phys. Rev. B - Condens. Matter Mater. Phys. 79 (2009) 153107. doi:10.1103/PhysRevB.79.153107.
- [55] M. Mussa, N.R. Mlyuka, M.E. Samiji, Hall Effect Parameters of Aluminium and Tungsten Co-Doped VO<sub>2</sub> Thin Films, Tanzania J. Sci. 44 (2018) 100–105. [www.ajol.info/index.php/tjs/](http://www.ajol.info/index.php/tjs/).
- [56] Y. Yang, Y. Yao, B. Zhang, H. Lin, Z. Luo, C. Gao, C. Zhang, C. Kang, Investigating metal-insulator transition and structural phase transformation in the (010)-VO<sub>2</sub>/(001)-YSZ epitaxial thin films, Materials. 11 (2018) 1713. doi:10.3390/ma11091713.
- [57] G.R. Khan, B. Ahmad, Effect of quantum confinement on thermoelectric properties of vanadium dioxide nanofilms, Appl. Phys. A Mater. Sci. Process. 123 (2017) 795. doi:10.1007/s00339-017-1363-x.
- [58] M.M. Qazilbash, M. Brehm, B.G. Chae, P.C. Ho, G.O. Andreev, B.J. Kim, S.J. Yun, A. V. Balatsky, M.B. Maple, F. Keilmann, H.T. Kim, D.N. Basov, Mott transition in VO<sub>2</sub> revealed by infrared spectroscopy and nano-imaging, Science. 318 (2007) 1750–1753. doi:10.1126/science.1150124.

- [59] Au crystal structure - SpringerMaterials.  
[https://materials.springer.com/isp/crystallographic/docs/sd\\_0261045](https://materials.springer.com/isp/crystallographic/docs/sd_0261045).
- [60] P. Hartel, H. Rose, C. Dinges, Conditions and reasons for incoherent imaging in STEM, *Ultramicroscopy*. 63 (1996) 93–114. doi:10.1016/0304-3991(96)00020-4.
- [61] A. Matthai, D. Ehrt, C. Rüssel, Voltammetric investigations of the redox behaviour of Fe, Ni, Co and Sn doped glass melts of AR and BK7 type, *Glas. Sci. Technol. Glas. Berichte*. 73 (2000) 33–38.
- [62] P. Bhagowati, M.B. Sahariah, Structure, stability and electronic properties of zirconium nitride nanoclusters, *Nanotechnology*. 35 (2024) 025701.  
doi:10.1088/1361-6528/ad00c3.
- [63] S. Yu, Q. Zeng, A.R. Oganov, G. Frapper, B. Huang, H. Niu, L. Zhang, First-principles study of Zr-N crystalline phases: phase stability, electronic and mechanical properties, *RSC Adv.* 7 (2017) 4697–4703. doi:10.1039/c6ra27233a.
- [64] D. Van Lam, H. Suematsu, T. Ogawa, Characterization of ZrN, ZrO<sub>2</sub> and  $\beta'$ -Zr<sub>7</sub>O<sub>11</sub>N<sub>2</sub> nanoparticles synthesized by pulsed wire discharge, *J. Am. Ceram. Soc.* 100 (2017) 4884–4892. doi:10.1111/jace.15012.
- [65] T. Bredow, M. Lerch, On the anion distribution in Zr<sub>7</sub>O<sub>8</sub>N<sub>4</sub>, *Zeitschrift Fur Anorg. Und Allg. Chemie*. 633 (2007) 2598–2602. doi:10.1002/zaac.200700281.
- [66] M. Protsak, P. Pleskunov, K.B.D. Nikitin, M. Tosca, A. Choukourov, Zirconium Nitride Nanoparticles Prepared by Reactive Magnetron Sputtering, *WDS'22 Proc. Contrib. Pap. — Phys.* (2022) 162–166.
- [67] D.B. Williams, C.B. Carter, *Transmission Electron Microscopy: A Textbook for Materials Science*, 2nd edition, Springer, New York, 2009.

- [68] C. Wang, L. Zhao, Z. Liang, B. Dong, L. Wan, S. Wang, New intelligent multifunctional SiO<sub>2</sub>/VO<sub>2</sub> composite films with enhanced infrared light regulation performance, solar modulation capability, and superhydrophobicity, *Sci. Technol. Adv. Mater.* 18 (2017) 563–573.  
doi:10.1080/14686996.2017.1360752.
- [69] Y. Arata, H. Nishinaka, M. Takeda, K. Kanegae, M. Yoshimoto, Strain-Induced Modulation of Resistive Switching Temperature in Epitaxial VO<sub>2</sub> Thin Films on Flexible Synthetic Mica, *ACS Omega*. 7 (2022) 41768–41774.  
doi:10.1021/acsomega.2c06062.
- [70] J. Jian, X. Wang, S. Misra, X. Sun, Z. Qi, X. Gao, J. Sun, A. Donohue, D.G. Lin, V. Pol, J. Youngblood, H. Wang, L. Li, J. Huang, H. Wang, Broad Range Tuning of Phase Transition Property in VO<sub>2</sub> Through Metal-Ceramic Nanocomposite Design, *Adv. Funct. Mater.* 29 (2019) 1903690. doi:10.1002/adfm.201903690.
- [71] C. Batista, R.M. Ribeiro, V. Teixeira, Synthesis and characterization of VO<sub>2</sub>-based thermochromic thin films for energy-efficient windows, *Nanoscale Res. Lett.* 6 (2011) 301. doi:10.1186/1556-276X-6-301.
- [72] M. Soltani, M. Chaker, E. Haddad, R. V. Kruzelecky, J. Margot, Effects of Ti-W codoping on the optical and electrical switching of vanadium dioxide thin films grown by a reactive pulsed laser deposition, *Appl. Phys. Lett.* 85 (2004) 1958–1960. doi:10.1063/1.1788883.
- [73] W. Burkhardt, T. Christmann, S. Franke, W. Kriegseis, D. Meister, B.K. Meyer, W. Niessner, D. Schalch, A. Scharmann, Tungsten and fluorine co-doping of VO<sub>2</sub> films, *Thin Solid Films*. 402 (2002) 226–231. doi:10.1016/S0040-6090(01)01603-0.

- [74] W. Wu, C. Wang, C. Chen, J. Song, F. Ma, Design of Antireflection and Enhanced Thermochromic Properties of TiO<sub>2</sub>/VO<sub>2</sub> Thin Films, *Adv. Mater. Interfaces*. 10 (2023) 2202506. doi:10.1002/admi.202202506.
- [75] B. Zhuang, Z. Dai, S. Pang, H. Xu, L. Sun, F. Ma, 3D Ordered Macroporous VO<sub>2</sub> Thin Films with an Efficient Thermochromic Modulation Capability for Advanced Smart Windows, *Adv. Opt. Mater.* 7 (2019) 1900600. doi:10.1002/adom.201900600.
- [76] C. Jiang, L. He, Q. Xuan, Y. Liao, J.G. Dai, D. Lei, Phase-change VO<sub>2</sub>-based thermochromic smart windows, *Light Sci. Appl.* 13 (2024) 255. doi:10.1038/s41377-024-01560-9.
- [77] Y. Cui, Y. Ke, C. Liu, Z. Chen, N. Wang, L. Zhang, Y. Zhou, S. Wang, Y. Gao, Y. Long, Thermochromic VO<sub>2</sub> for Energy-Efficient Smart Windows, *Joule*. 2 (2018) 1707–1746. doi:10.1016/j.joule.2018.06.018.
- [78] I. Alonzo-Zapata, C. Champeaux, F. Enguehard, J. Ordonez-Miranda, F. Dumas-Bouchiat, Emissivity Measurements of Vanadium Dioxide Thin Films through the Thermal Wave Resonant Cavity and its Applications in Radiative Thermal Diode and Transistor Simulations, *Int. J. Heat Mass Transf.* 224 (2024) 125298. doi:10.1016/j.ijheatmasstransfer.2024.125298.